Large-scale failure prediction of clay rock from small-scale damage mechanisms of the rock medium using multiscale modelling

Christos Mourlas, Benoît Pardoen, Pierre Bésuelle

Large-scale failure prediction of clay-rock from small scale damage mechanisms of the rock medium using multiscale modelling

SCHOLARONE™
Manuscripts

Large-scale failure prediction of clay rock using multiscale modelling

Large-scale failure prediction of clay rock from small scale damage mechanisms of the rock medium using multiscale modelling

Christos Mourlas[1,2*], Benoît Pardoen[1], and Pierre Bésuelle[3]

[1]Université de Lyon, ENTPE, LTDS, 69120 Vaulx-en-Velin, France
[2]Faculty of Civil Engineering, Czech Technical University in Prague, Thákurova 7, 166 29 Prague, Czech Republic (current affiliation)
[3]Université Grenoble Alpes, CNRS, Grenoble INP, 3SR, 38000 Grenoble, France
[*]Corresponding author: christos.mourlas@fsv.cvut.cz

Abstract

Clay rocks are multiphase porous media whose complex structure is characterised by heterogeneity and possible anisotropy on a wide range of scales. The mesoscopic scale plays a particular role in deformation mechanisms under mechanical loading by cracking. The behaviour of rocks at mesoscale is characterised by the material and morphological (shape and size) properties of its components and their interactions. The accurate reproduction and influence of these mesoscale characteristics on the material behaviour and damage at large scale remain a complex issue. This question becomes crucial when investigating the underground stability during excavation works such as tunnels. In this numerical multi-scale study, the mesostructure characteristics are embedded in a Representative Elementary Area (REA) in a 2D configuration. A double-scale numerical framework, with finite element resolution at both scales (FE²) and computational homogenisation, is considered. The influence of the mesostructural characteristics of a heterogeneous rock and the effect of different inter-granular properties on their macroscopic behaviour, are examined. Additionally, a predictive strategy which is based on the connection between the failure modes of the REA and the failure mechanisms of the macroscale structure is also presented. This study investigates the effect of the mesocracking on the shear banding in a rock specimen during laboratory biaxial shear test and the development of the Excavation Damaged Zone (EDZ) around tunnels. The objective of this work, is to explain the failure mechanisms observed up to the engineering scale of underground structures through the morphological and material small-scale characteristics of the REA.

Keywords

Shear failure, mesoscale modelling, mineral morphology, double-scale analysis, REA, EDZ.

1. Introduction

The geomaterials in the vicinity of underground structures, such as soils and rocks, are multiphase porous media with a generally complex structure that can extend over several scales [1]. In this research, the underground tunnels are considered as deep geological repositories of nuclear wastes. Among materials suitable for deep geological repository of nuclear wastes, clayey rocks are considered in particular for their low intrinsic permeability [2–4]. The Callovo-Oxfordian claystone is studied as the potential host rock selected in France by the French national radioactive waste management agency Andra [2]. The complex structure of the material that includes the heterogeneity, the anisotropy and the spatial variability of characteristics, indicates the necessity of investigating its behaviour at different scales, depending to the studied phenomena. Short-term deformation, especially in excavated damage zone (EDZ) around gallery, induces micro-fissuring mechanisms on a multi-micrometer scale, the meso-scale of mineral inclusions imbedded in a clay matrix. This fissuring mechanism can be a major factor in the variation of material permeability [5]. The analysis of material behaviour at this scale (i.e. micrometric) is nowadays a major objective in (geo) mechanics to explain and model the mechanisms

1

observed on a larger scale, and to enrich constitutive behaviour models. The complexity of the behaviour of geomaterials as rocks is related to several aspects on different scales as a complex microstructure, the appearance of complex strain localisation pattern before material rupture, and the existence of several multiphysics couplings [1,6,7]. It has to be noted that the microscale is referring here to a sub-micrometer scale that consists of a mixture of clay particle or aggregates. However, the macroscopic scale is the scale of the characteristic size in the sub-millimetre range.

The influence of small-scale characteristics on the damage and stability of underground structures remains a complex problem difficult to investigate in the field of underground constructions [7]. Its understanding is crucial to ensure the feasibility of constructing and operating safe structures. Consequently, the main goal of this research study is the modelling of multi-scale damage of clay rocks and its influence on deep tunnel stability.

The definition of macroscopic behaviour is generally achieved through the use of phenomenological constitutive laws. However, to represent and model more accurately the material behaviour, various scientific questions have been raised on how mesostructural characteristics of heterogeneous geomaterials can enrich macroscale constitutive behaviour models [1,8–11]. In this spirit, multiscale methods relying on computational homogenisation techniques have been developed [12–15]. The objective of such approach is to "transfer" mesostructural information to upper scales, considering the characteristic dimensions of the considered phenomenon. The objective being to provide output at macroscale by upscaling approach. This includes the "extraction" of a behaviour law from the micro-or meso- structural scale (grains/minerals and porous network scale) to the macroscopic scale. Among the numerical homogenisation approaches suitable for heterogeneous geomaterials, a finite element method is used at both small- and large- scales (FEM^2 technics), including hydro-mechanical couplings at the mesoscale.

The current study aims to investigate how the mesostructural characteristics of the Callovo-Oxfordian clay rock can affect the macrostructural behaviour through a proposed prediction strategy of (meso-to-macro) shear failure. The proposed model used in this study, describes the small-scale as a clay matrix with non-clayey grains in an area with a characteristic length ≈ 105 μm and thus, it is considered to be in meso-scale. At small-scale, in a randomly generated Representative Elementary Area (REA), a random distribution of the mineral inclusions generates a random distribution of mineral contacts [7,16]. These mineral contacts represent the possible location of meso-crack development (grain debonding from mineral phases and intra-phase fissuring) [7,16]. Therefore, the mineral contact distribution shows the possible mesocracking path that it is going to develop (by mesocracks coalescence between the mineral inclusions) through the REA model. Additionally, the mesocracking path shows the tendency of the material preferred shear crack direction. This indication is crucial since it is connected to specific macroscale shear failure mechanisms and to the material macroscale anisotropic response. Hence, the current research is focused on the connection between the mesocracking and the macro-failure mechanisms at meso- and macro- scales, respectively.

The predictive capabilities of the proposed predictive methodology are applied to REAs having different sizes, from less to more representative of the material mesostructure. These REAs are mechanically solicited to capture the clay rock shear behaviour under deviatoric loading (biaxial compression) in mesoscale and double-scale analysis. Finally, these REAs are also used to model the EDZ that develops in the clay rock around underground galleries. The effect of the different failure mechanisms around the gallery and its connection to the failure of the REA is examined. Additionally, various studies with different REAs which produce different failure mechanisms (at meso- and macro-scales) are presented. It has to be noted that the presented study focuses on the mechanical behaviour of clay rock material.

2. *Callovo-Oxfordian clay rock*

The current study intends to numerically reproduce the behaviour of the Callovo-Oxfordian clay rock (COx). This rock is considered by Andra (the French national radioactive waste management

2

Large-scale failure prediction of clay rock using multiscale modelling

agency) as a potential host rock for the repository of nuclear waste, thanks to its low permeability and retaining capabilities of radionuclides. The rock damage induced by the underground excavation process can affect the safety of underground repository facilities. Andra developed an Undergroung Research Laboratory (URL) at approximately 490 m below ground surface which corresponds to the median depth of the COx formation [2].

During the excavation processes, different modes of fracture take place in the surrounding medium: opening or tensile fractures (mode I), shear fractures (mode II), and the combination of the two previous ones [6]. The distributed damage that appears near the drift wall constitutes the excavation damaged zone (EDZ) which is a zone characterised by geomechanical and hydro-mechanical property alterations [17,18]. In this article, the excavation damage zone (EDZ) in COx claystone is studied and its relation to the failure types in mesoscale.

The microstructure of the COx clay rock is heterogeneous and composed of several types of minerals: tectosilicates (-Si_xO_y, mainly quartz, 10-40%), carbonates (-CO_3, mainly calcite, 15-80%), heavy minerals (FeS_2, pyrite in a low proportion of 0-3%) and clay minerals (20-60%) [2,6,19,20]. The experimental analysis methods on micro- and meso- structures (e.g. Scanning Electron Microscopy SEM, X-ray micro-Computed Tomography, image analysis, etc.) have led to the definition of the different mineral groups, their spatial distributions, mineral area fractions, as well as size, shape, and orientation of the mineral inclusions. The detailed results of these analyses for the COx clay rock can be found in other works [20,21,22]. The above experimental evidence shows that potential decohesion mechanisms can develop around mineral inclusions and micro-cracks within the clay matrix.

3. *Double-scale model*

Among the computational homogenisation approaches, finite element methods (FEM) are often used at larger scale combined with various numerical approaches at smaller scale [12,15,23–25]. From a constitutive point of view, multiscale methods allow a scale transition (based on the notion of scale separation) for which the homogenised small-scale response (e.g. mesoscopic) serves as an implicit constitutive law at larger scale (e.g. macroscopic by computational homogenisation). Numerical mesostructural models (usually periodic) generally require the definition of a Representative Volume Element (RVE) and its boundary conditions to define the behaviour of the mesostructure. At micro- and meso-scopic scales in geomaterials, RVEs represent solid constituent assemblages and include their micromechanical properties. Multiphysical couplings (e.g. hydromechanical) can be considered at the small scale, then the introduced relative complexity can induce a richness of the macroscopic behaviour which is difficult to be obtained by phenomenological laws (anisotropy, cyclic behaviour, etc.). Obviously, such double-scale numerical methods require model validation, intensive scientific computing, and high-performance parallelisation of computation code.

Various multiscale methods (e.g. with FEM or finite volume methods) have been developed to accurately describe solid behaviour and fluid transports (e.g. composite materials, subsurface flow in heterogeneous porous media, etc.) [26]. Other multiscale FEM studies focus on the heterogeneous medium, permeability variation, structures with random porosity structures or internal crack, studies include simulation problems in fractured porous media, of transport problems. An exhaustive literature review about the above topics is presented in Zhang et al. [27]. For other (civil) engineering applications, the mechanical behaviour of advanced composite materials [28,29] and multi-layered anisotropic structures [30] has also been modelled though multiscale approaches. Specifically, for geomaterials, macroscale FEM are often combined with discrete or finite element methods (respectively, DEM or FEM) at smaller scale, depending on the structure at small scale. Thus, FEMxDEM and FEMxFEM (or FE²) methods are often used for rocks and soils [7,15,25].

In the next sections, a brief description of the FE² method which is used to model accurately the heterogeneous COx clay rock by describing several types of minerals with different sizes, shapes, orientations, and mineral-contact decohesion mechanisms, is presented.

3.1. **Macroscale model**

3

Large-scale failure prediction of clay rock using multiscale modelling

In the used FEM[2] method, the constitutive behaviour at each integration point in the macroscale finite element computation is derived from a boundary value problem (BVP) on a representative elementary area (REA) at the mesoscale, including hydro-mechanical couplings. The methods are described in detail in other works [14,15]. A brief description of the model is summarised hereafter for the sake of completeness.

On the macro-scale, the rock shear failure is reproduced by strain localisation in shear band mode, as a precursor of shear fracture. A second gradient model (regularisation method) is used in order to describe the equilibrium under quasi-static conditions for the field variables of displacement u_i and fluid pressure p_w. The consideration of this regularisation method is required in order to properly model the phenomenon of strain localisation, by introducing an internal length scale and by avoiding mesh dependency [15,31–33]. Therefore, the classical kinematics are enhanced with the microkinematical gradient v_{ij} which describes the microstructure kinematics. This gradient is assumed to be equal to the gradient of the macro displacement $v_{ij} = \partial u_i / \partial x_j$ according to the second gradient theory [34–37]. Additionally, this kinematic restriction is introduced through a field of Lagrange multipliers λ_{ij} related to a weak form of constraint [36] in order to make the displacement field of the second gradient model a continuously differentiable function. Therefore, the field equations of the numerical coupled problem for every kinematically admissible virtual displacement field u_i^* and pore water pressure field p_w^* are:

$$\int_{\Omega^t}\left(\sigma_{ij}^t\frac{\partial u_i^*}{\partial x_j^t} + \Sigma_{ijk}^t\frac{\partial v_{ij}^*}{\partial x_k^t}\right)d\Omega^t - \int_{\Omega^t}\lambda_{ij}^t\left(\frac{\partial u_i^*}{\partial x_j^t} - v_{ij}^*\right)d\Omega^t = \int_{\Omega^t}\rho^t g_i u_i^*\,d\Omega^t + \int_{\Gamma_\sigma^t}\left(\bar{t}_i^t u_i^* + \overline{T}_i^t v_{ij}^* n_j^t\right)d\Gamma^t \tag{1}$$

$$\int_{\Omega^t}\lambda_{ij}^*\left(\frac{\partial u_i^t}{\partial x_j^t} - v_{ij}^t\right)d\Omega^t = 0 \tag{2}$$

$$\int_{\Omega^t}\left(\dot{M}_w^t p_w^* - f_{w,i}^t\frac{\partial p_w^*}{\partial x_i^t}\right)d\Omega^t = \int_{\Omega^t}Q_w^t p_w^*\,d\Omega^t - \int_{\Gamma_{qw}^t}\bar{q}_w^t p_w^*\,d\Gamma^t \tag{3}$$

where x_i^t are the current coordinates, the general notation of a^* corresponds to the virtual quantity a, v_{ij}^* is the virtual microkinematic gradient, and Σ_{ijk}^t is the double stress dual of the virtual micro second gradient. Furthermore, $\bar{t}_i^t$ is the classical external traction force per unit area, $\overline{T}_i^t$ is an additional external double force per unit area, both applied on a part Γ_σ^t of the boundary Γ^t of Ω^t, n_k^t is the normal unit vector to the boundary, ρ^t is the mixed solid and fluid mass density (kg/m³), $\dot{M}_w^{\,t}$ is the liquid water mass variation in the current configuration, $f_{w,i}^t$ the liquid water mass flow, Q_w^t a water sink term, and $\bar{q}_w^t = f_{w,i}^t n_i^t$ the input water (positive for inflow) mass per unit area on a part Γ_{qw}^t of Γ^t.

According to above equations, a first constitutive relation has to establish the relation between the classical (Cauchy) stress and strain which is treated here by the computational homogenised FEM[2] model. Because hydromechanical couplings are introduced at the mesoscale, this one also provides the link between pore pressure and water mass, as well as the pressure gradient and fluid flow. An additional constitutive law has to be established for the double stress Σ_{ijk} and micro deformation. For simplicity reasons, a linear elastic mechanical law is used, derived by Mindlin [34]. Thus, the relation between double stress Σ_{ijk} and double strain $\partial v_{ij}/\partial x_k$ depends only on one constitutive elastic parameter D and it is related to the internal length scale relevant for the shear band width [36,38,39,45]. It has to be clarified that, although the terms "microkinematics" and "micro deformation" are used above, following the formalism of Germain [35], the lowest scale in the presented approach considers to be in the mesoscale.

The macroscale finite elements that are used in this study are 2D quadrilateral elements (9 nodes, 4 integration points) under plane strain conditions [32] implemented in the finite element code Lagamine [40] from University of Liège (Belgium).

Large-scale failure prediction of clay rock using multiscale modelling

3.2. **Mesoscale model**

The mesostructure of the clay rock is described by a two-dimensional Representative Elementary Area (REA). It consists of elastic deformable continuous (non-porous) solid minerals separated by damageable cohesive interfaces. Through these interfaces the model can reproduce meso-damage and intergranular failure (i.e. clay matrix mesocracking and mineral inclusion decohesion) as observed in Desbois et al. [5]. This model is based on the microscale model (or mesoscale model in this study) developed initially by Frey et al. [14] and modified then by van den Eijnden et al. [15].

The mesoscale model serves as the constitutive model of the macroscale simulation. In order to connect the two scales (Macro- and meso-), appropriate boundary conditions have to be established on the periodic REA. In this study, periodic external boundary conditions are used (Figure 1 (a)), where the relative displacement between opposite external boundaries of the REA is enforced following:

$$du_i^{t,m} = \varepsilon_{ij}^{t,M} y_j^t \tag{4}$$

where $du_i^m = u_i^{m,F} - u_i^{m,L}$ is the differential boundary displacement at mesoscale, ε_{ij}^M is the gradient of macro-displacement, and $y_j = x_j^F - x_j^L$ is the mesoscale boundary periodic vector. $x_j^F - x_j^L$ and $u_i^{m,F} - u_i^{m,L}$ are the homologous couples of coordinates and displacements on the periodic REA boundary Γ (F stands for Follower and L for Leader). Moreover, the boundary traction surface forces t_i on opposite mesostructure boundaries is antisymmetric. For the internal mineral boundaries (Figure 1 (b)), upper and lower boundaries Γ^{int+} and Γ^{int-} are defined, where the reciprocal cohesive forces c_i^+ and c_i^- act on the corresponding displacements u_i^+ and u_i^-, leading to a displacement discontinuity $\Delta u_i = u_i^+ - u_i^-$ across the interface. The balance of momentum equation of the mesoscale boundary value problem is written in the weak form, for any kinematically admissible virtual field of displacement $u^{*,m}$, as follows (the gravity effect is considered negligible):

$$\int_{\Omega_{EA}} \left(\sigma_{ij}^{t,m} \frac{\partial u_i^{*,m}}{\partial x_j^t} \right) d\Omega^t = \int_{\Gamma_{int}^+} c_i^{t,+} u_i^{*,m,+} d\Gamma^t + \int_{\Gamma_{int}^-} c_i^{t,-} u_i^{*,m,-} d\Gamma^t \tag{5}$$

For the solution of the above equation, two-dimensional four-nodes isoparametric quadrilateral FEs (with four integration points) are used. Additionally, the interface is discretised with four nodes FEs with zero thickness [15]. Specifically, the cohesive forces as shown in the Figure 1 can be characterised as normal and tangential cohesive forces, i.e. c_n and c_t, which are related to the corresponding normal and tangential relative displacements, i.e. u_n and u_t by the interface constitutive law. It has to be noted that a decoupling between normal and tangential components is assumed for simplification. The damage law is described by the following three parameters:

i. The maximum cohesion, $c_{t/n}^{max}$

ii. The softening or damage parameter corresponding to the relative degradation of the contact cohesion, $0 \leq D_{t/n}^t \leq 1$

iii. The critical relative displacements for complete decohesion, $\delta_{t/n}^c$ ($c_{t/n} = 0$, $D_{t/n} = 1$).

where n and t subscripts correspond to the normal and tangential directions.

(a)   (b)

5

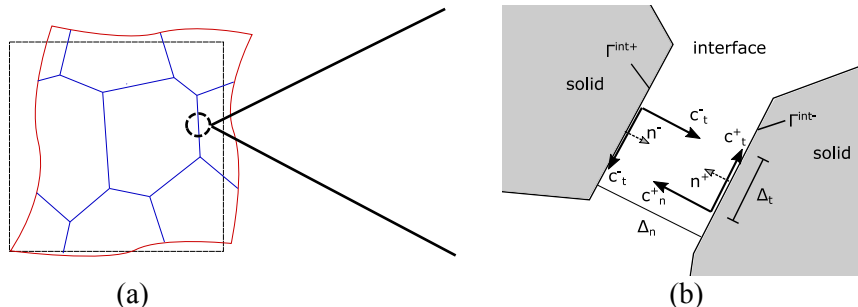*Large-scale failure prediction of clay rock using multiscale modelling*

1 *Figure 1. Mesostructure model (REA): (a) periodically deformed configuration and (b) cohesive interface forces*
2 *acting on the boundaries of two solids in contact (adapted from van den Eijnden et al.[15]).*

3   The constitutive laws for the normal and tangent interface cohesions are defined with the
4 following expressions:

$$c_n^t = \begin{cases} c_n^{\max}\left(1-D_n^t\right)\dfrac{1}{D_n^t}\dfrac{\Delta u_n^{m,t}}{\delta_n^c} & \text{if } \Delta u_n^{m,t} \geq 0 \\[2ex] c_n^{\max}\left(1-D_n^t\right)\dfrac{1}{D_n^t}\dfrac{\Delta u_n^{m,t}}{\delta_n^c} - \kappa\left(\Delta u_n^{m,t}\right)^2 & \text{if } \Delta u_n^{m,t} < 0 \end{cases} \tag{6}$$

$$c_t^t = c_t^{\max}\left(1-D_t^t\right)\dfrac{1}{D_t^t}\dfrac{\Delta u_t^{m,t}}{\delta_t^c} \tag{7}$$

5 where $\Delta u_{t/n}^{m,t}$ are the non-dimensional interface relative displacements (relative to the unit EA size) at time
6 t and κ is a penalisation term to avoid mineral inter-penetration. Furthermore, the interface state
7 parameter $D_{t/n}^t$ is related to the critical relative displacement $\delta_{t/n}^c$ and the history ($\tau = 0 \mathsf{K}\ t$) of the relative
8 displacement $\Delta u_{t/n}^m$. It is defined for the normal and tangential displacement separately, with the following
9 expressions:

$$D_n^t = \begin{cases} \max\left(D_n^0, \dfrac{1}{\delta_n^c}\max_{0\leq\tau\leq t}\left(\left|\Delta u_n^{m,\tau}\right|\right)\right) & \text{if } \Delta u_n^{m,\tau} \leq \delta_n^c \\[2ex] 1 & \text{if } \delta_n^c < \Delta u_n^{m,\tau} \end{cases} \tag{8}$$

$$D_t^t = \begin{cases} \max\left(D_t^0, \dfrac{1}{\delta_t^c}\max_{0\leq\tau\leq t}\left(\left|\Delta u_t^{m,\tau}\right|\right)\right) & \text{if } \left|\Delta u_t^{m,\tau}\right| \leq \delta_t^c \\[2ex] 1 & \text{if } \delta_t^c < \left|\Delta u_t^{m,\tau}\right| \end{cases} \tag{9}$$

10   A schematic representation of the linear damage models in the normal and tangential directions
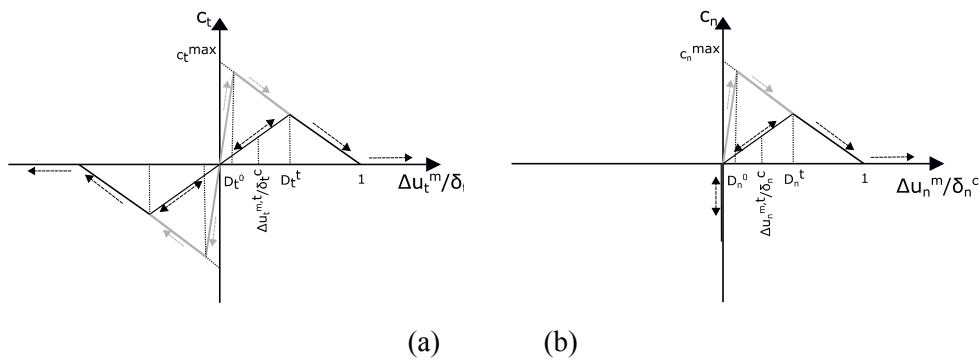11 to the mineral boundaries are illustrated in Figure 2.

(a)   (b)

12 *Figure 2. Linear damage constitutive models for interface cohesion for: (a) tangential and (b) normal directions*
13 *(adapted from van den Eijnden et al.[15]).*

14   For completeness of the description of the theoretical part of the modelling approach, it has to
15 be added that the solid minerals in the mesoscale are considered impervious and the pore channel
16 network is formed by the mineral interfaces. The latter allow the fluid to be transported as a reaction to
17 a pressure gradient. In this numerical approach, an assumption of steady-state laminar flow between
18 smooth parallel plates (interface sides) is made. The interface opening, which controls the fluid flow,
19 can take a minimum value (and an initial one) in order to account for the bulk permeability of undamaged
20 material of low permeability. All these aspects of the model are described in detail in van den Eijnden
21 et al.[15]. Therefore, in case of the intact material, the homogenised permeability is assured. The fluid

6

Large-scale failure prediction of clay rock using multiscale modelling

mass flux $\overline{\omega}^t$, at a certain position s in the channel, is calculated through a relation of the fluid dynamic viscosity μ, the interface hydraulic opening Δu_h^t, the water pressure gradient dp_w^*/ds^t, and the liquid fluid density $\rho^{w,t}$ with the following expression:

$$\overline{\omega}^t = -\rho^{w,t}\frac{12}{\mu}\Delta u_h^{t\,3}\frac{dp_w^*}{ds^t} \tag{10}$$

3.3. Computational homogenisation

After the solution of the boundary value problem of the REA, the homogenised macroscale response in terms of the total stress tensor σ_{ij} is derived from Hill-Mandel macro-homogeneity condition [41,42] which describes equal (virtual) work at both scales. Therefore, the computational homogenisation is used in order to transmit different values from mesoscale to macroscale (upscaling). It has to be noted that the homogenisation of the consistent tangent operators is succeeded by using static condensation procedure [13] as described in van den Eijnden et al. [15]. The homogenised total stress tensor is the average stress over the REA and it is defined by the following expression:

$$\sigma_{ij}^{t,M} = \frac{1}{\Omega_{EA}^t}\int_{\Gamma^{F,t}} t_i^t y_j^t d\Gamma^t \tag{11}$$

where t_i are the REA boundary traction surface forces on the REA boundary Γ^F. Similarly, the macroscale flux and the specific fluid mass can be expressed as:

$$m_i^{t,M} = \frac{1}{\Omega_{EA}^t}\int_{\Gamma^{F,t}} q_i^t y_j^t d\Gamma^t \tag{12}$$

$$M^{t,M} = \frac{1}{\Omega_{EA}^t}\int_{\Omega_{EA}^{h,t}} \rho^{w,t} d\Omega^t \tag{13}$$

where, q_i^t is the boundary flux on REA boundary Γ^F, $\rho^{w,t}$ is the fluid density and $\Omega_{EA}^{h,t}$ indicates the part of the whole domain occupied by the fluid phase. A schematic representation of the whole double scale procedure considering the REA in mesoscale and the computational homogenisation is illustrated in Figure 3.
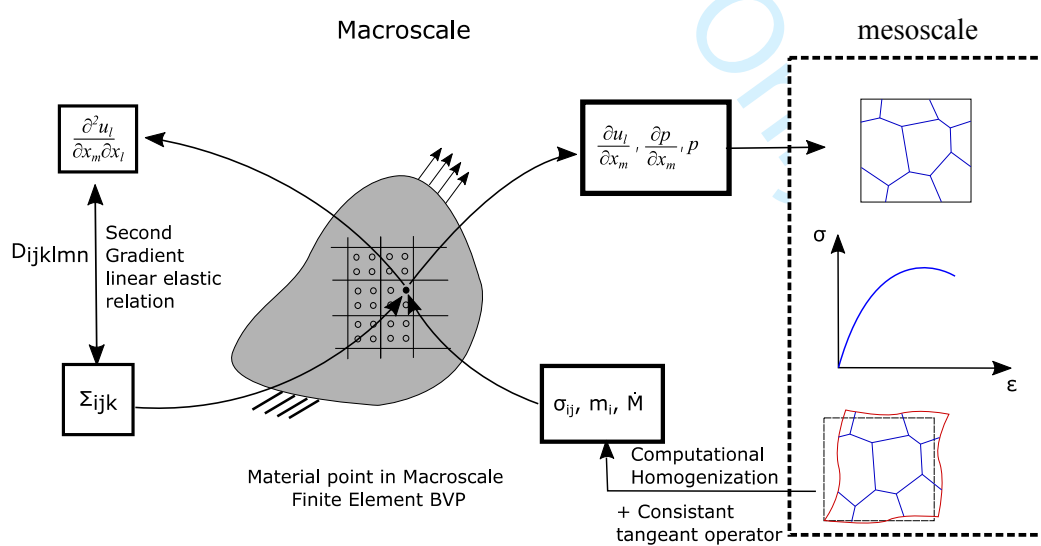

Figure 3. Schematic representation of the FE² method for hydromechanical coupling with a local second gradient model (adapted from van den Eijnden et al. [7]).

7

Large-scale failure prediction of clay rock using multiscale modelling

4. *Mesostructure characteristics*

The current section describes briefly the generation algorithm of heterogeneous mesostructure that mimics the real microstructure of COx clay rock. The algorithm uses a 2D Voronoï tessellation procedure in which the cells of the REA represent either large clay aggregates of the clay matrix, either mineral inclusions (Figure 4). The algorithm considers the main morphological characteristics of the COx clay rock [7,16]. The latter are: the roundness, the elongation, the orientation, the size of the mineral inclusions, the area fractions of the mineral phases, and the characteristic size of the REA. The procedure allowing to generate realistic mesostructures (in the clay-rich zone of the rock) is described in Pardoen et al. [16]. Furthermore, the size of the RVE is measured experimentally and it is found to be $V_{RVE} \approx 0.001\, mm^3$, which corresponds to a representative length of $L_{RVE} \approx 100\, \mu m$ [21,22]. According to Pardoen et al. [16], this representative size is reproduced numerically by REA with 250 Voronoï cells. An example of representative REA is illustrated in the Figure 4. The deformed configuration of the REA under deviatoric biaxial compression (in Figure 4 (b)) shows the damaged interface state of the mineral (cells) contacts where the softening state corresponds to the softening or damage parameter $0 \leq D_{t/n}^t \leq 1$, while the fully damaged (decohesion) state corresponds to $D_{t/n}^t = 1$ as illustrated in Figure 2. The interfaces between the "grains" of the mesostructure are considered to be the preferred paths of mesofissure. They can represent either intra-phase cracking (e.g. cracking in the clay phase if it is an interface between two large clay aggregates) or mineral inclusion decohesion (e.g. debonding of a quartz inclusion from the clay matrix).
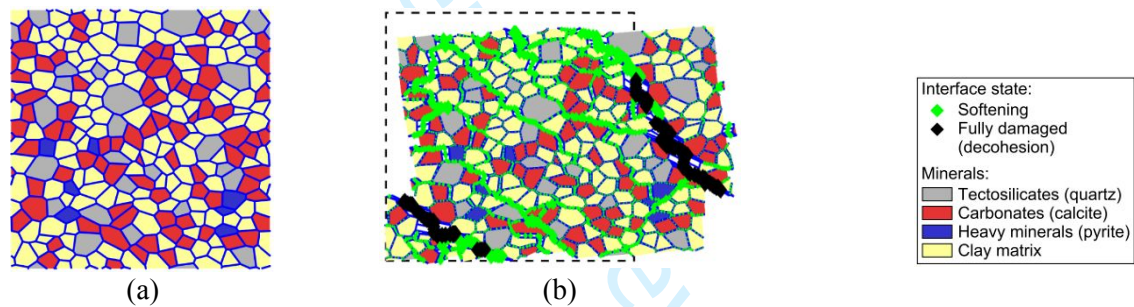

Figure 4. Schematic representation of a representative mesostructure (REA) with its components in its (a) undeformed and (b) deformed configurations under deviatoric biaxial compression.

The material parameters that are used in this study, are the elastic properties of calcite (carbonates), quartz (tectosilicates), and pyrite (heavy minerals). The properties and the percentages of the mineral components that are used, within the mesoscale REA model, are presented in Table 1. The mineral contact properties are considered as homogeneous, in a simplifying assumption [16]. The mineral interface parameters and the elastic properties of the clay matrix were calibrated using the homogenised response (of REA) in comparison with laboratory tests [7,16].

Table 1. Microscale mechanical parameters [16].

Minerals	E (GPa)		v (-)		%
Tectosilicates (quartz)	95		0.074		18
Carbonates (calcite)	84		0.317		30
Heavy minerals (pyrite)	305		0.154		2
Clay matrix	2.3		0.110		50
Interfaces	$\delta_{t/n}^c$ (-)	$D_{t/n}$ (-)	c_t^{max} (MPa)	c_n^{max} (MPa)	
	0.1	0.001	2.5	1.0	

Large-scale failure prediction of clay rock using multiscale modelling

5. Prediction of shear failure from meso- to macro- scales

The shear failure of the Callovo-Oxfordian clay rock across scales is modelled hereafter. It is predicted from mesocracking, within the clay matrix and between mineral inclusions, to larger-scale fractures, as those observed on laboratory rock samples (pluricentimetric scale) and around underground excavations (plurimetric scale). In order to illustrate how the anisotropy resulting from the morphology of a REA can influence the macroscopic behaviour and more particularly the localisation of the macroscopic deformation, a mesocrack-prediction strategy (based on the REA geometry) is proposed for rock mesostructures subjected to deviatoric biaxial compression. Then, the effects of mesocracking on macro-shear banding development are analysed on larger laboratory samples. The shear fracture process that develops at macroscale is numerically represented by strain localisation in shear bands (continuous approaches) (Pardoen et al. [43]). Fracturing around underground gallery is studied in section 6.

5.1. Mesoscale geometrical analysis

5.1.1. Biaxial compression

The numerical model of the biaxial compression test of the REA under 2D plane-strain state is defined in Figure 5. The vertical displacement of the bottom corners of the REA is blocked and the displacement of a corner node is blocked in both directions to avoid rigid body displacement. The biaxial compression is performed by applying firstly an isotropic confining pressure σ_{11} on the external boundary Γ of the REA, then a deviatoric phase by increasing progressively the vertical strain ε_{22} on the top surface of the REA. This leads to an increase of deviatoric load q. For the considered triaxial loading test, the deviatoric loading is equal to the differential one: $q=\sigma_{22}-\sigma_{11}$. Concerning the hydraulic conditions, the clay rock is considered in a water saturated state without considering pore water over-pressures (globally drained condition with constant p_w on the REA external boundary Γ). Results in terms of (q-ε_{22}) homogenised REA response curve and meso-cracking developments are available in Pardoen et al. [16].

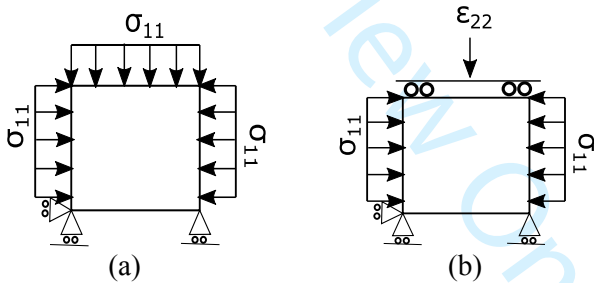*Figure 5. Numerical model of a plane-strain biaxial compression performed on a mesostructure: (a) isotropic loading and (b) deviatoric loading.*

5.1.2. Prediction algorithm

A new method based on REA morphology analysis is proposed in order to estimate and predict the dominant orientation of coalesced meso-cracking pattern that may develop through the REA. This ultimate damage process at the mesoscale is often activated in areas of high deformation, e.g. in the localisation bands. Therefore, it is quite expected that the preferential orientation of the damage itself influences the orientation of the localization bands at the macroscopic scale. The prediction strategy derives from the idea that the contact morphology of the solid minerals, composing the clay rock mesostructure in this numerical approach, could have a key role on the material mechanical response and cracking under deviatoric compressive loading conditions. This will be investigated numerically. It should be noted that this analysis only makes sense if all interface properties are identical, which is assumed here, for simplicity. This assumption is tested, as can be seen in Figure 6, where a REA (composed of 250 numerical-mineral cells, $L_{REA}\approx100\mu m$) with the same cell distribution (and same geometry of the interfaces) but with different mineral property distributions is examined under

9

deviatoric stress loading (i.e. biaxial compression test as illustrated in Figure 5). It can be seen that the mesocrack patterns, when the vertical strain is equal to $\varepsilon_{22} = 0.1$ and the REAs are reaching failure, are very similar. It confirms that the developments of mesocrack patterns, within numerical mesostructures (REA) under deviatoric loading, are not affected significantly by the mechanical properties of the minerals. Therefore, the mesostructural shear failure behaviour of the presented numerical model is dominated by the geometrical and morphological characteristics of the REA.
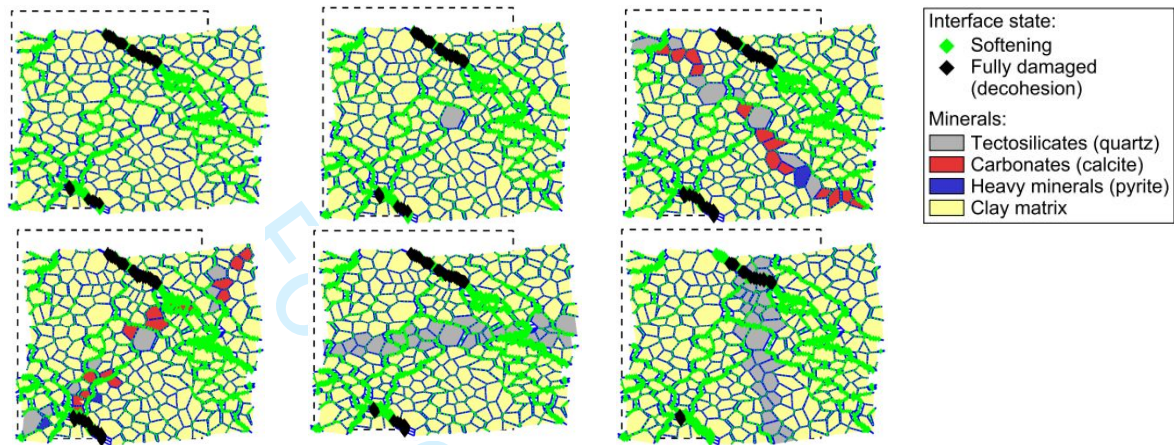

Figure 6. Mesocrack patterns in REAs, having reached shear failure, with the same cell distribution but with different mineral property distributions under a biaxial compression test.

The mesostructure shear strength corresponds to the deviatoric stress peak $q_{max}=max(q)=max(\sigma_{22}-\sigma_{11})$ of the homogenised stress-strain response curve. At this stress peak, a coalesced mesocrack pattern develops through the entire REA [16] that leads to the mesostructure shear failure. The orientation of this meso-fault conditions the REA shear deformation and its anisotropic character. Furthermore, the meso-fault pattern changes as the random distribution of the numerical-mineral cells (i.e. the morphology of the REA) changes. As aforementioned, periodic boundary conditions of REAs constrains the mesostructure shear failure pattern that has to be periodic itself. Therefore, a particular focus is given to the effect of the random positions of interface elements on the development of the REA mesocracking. The investigation starts by examining REAs with representative size of $L_{REA}\approx100\mu m$ (250 cells) [16].

The first step is to detect the positions and the orientations of all interface elements and to categorise them according to their orientation. For this purpose, each REA is sub-divided into several sub-square zones where interface elements are grouped to be analysed. Then, in each square zone, the orientations, the lengths, and the number of the interface elements are calculated. The location of each interface element is defined by the coordinates of their centre point. A schematic representation of this process is depicted in Figure 7 (a).
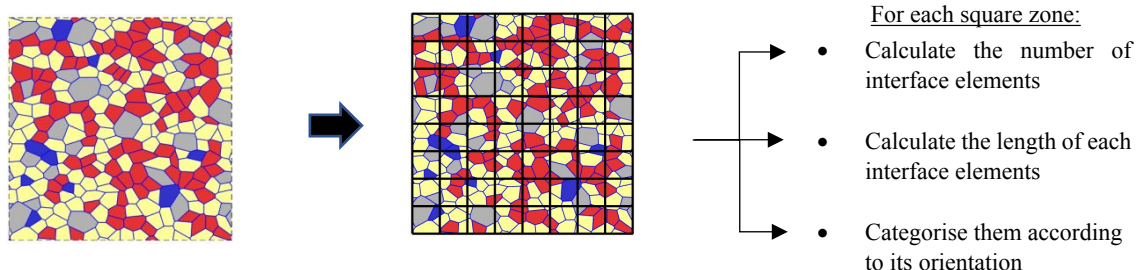
(a)

Large-scale failure prediction of clay rock using multiscale modelling

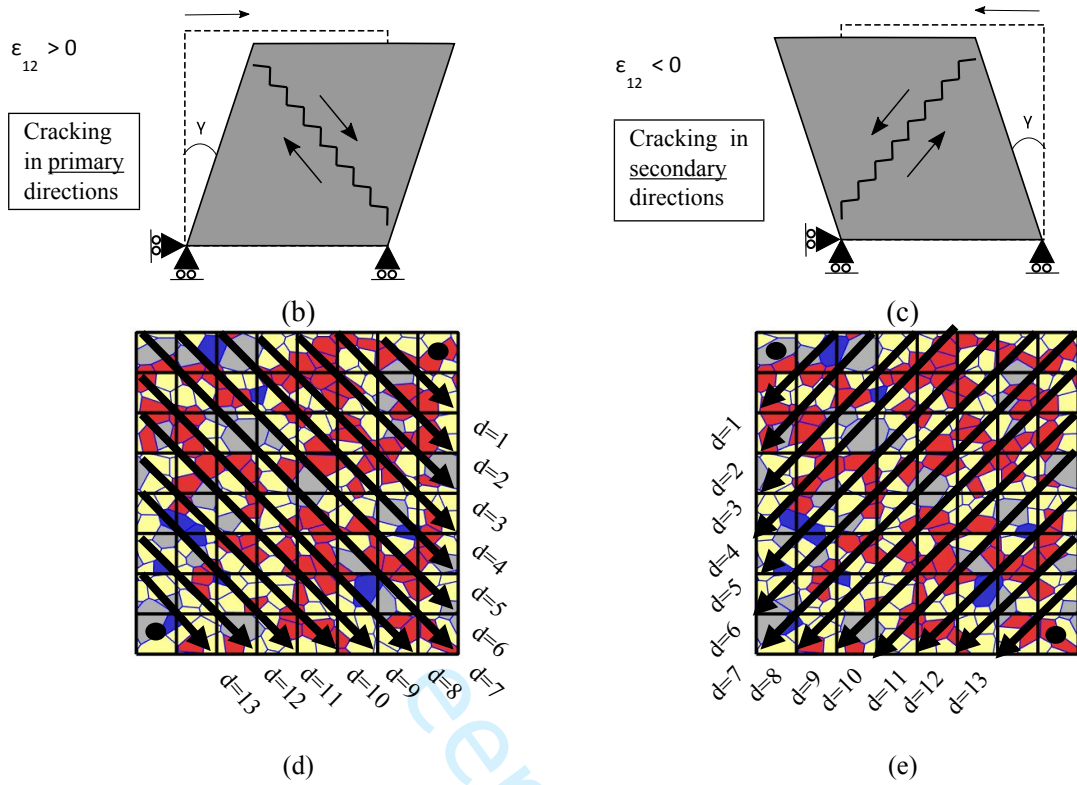(b)   (c)

(d)   (e)

Figure 7. Mesocrack prediction: (a) presentation of the algorithm, (b,c) schematic representation of two possible main mesocrack directions of a REA under simple shear conditions, and (d,e) determination of the possible mesocrack path.

In order to categorise the interface elements in terms of their orientation, relative to the horizontal direction, it is chosen to separate them into 4 intervals: $[0°\text{-}22.5°]$, $[22.5°\text{-}45°]$, $[45°\text{-}67.5°]$, and $[67.5°\text{-}90°]$ (even with more intervals, the conclusions about the dominant orientation tendency of the main shear mesocrack development remain the same). This differentiation is needed in order to distinguish two main directions of mesocrack developments through the REAs. For simplicity the case of simple shear is illustrated in Figure 7 (b,c) in order to show the connection of two possible crack diagonal directions in the REA with its corresponding global deformation (and homogenised shear strain ε_{12}).

Therefore, the possible crack path (P), for each square zone (c), for each interval-angle category (a, a=1,2,3,4 which corresponds to the 4 intervals), and for each crack direction (primary or secondary, according to Figure 7 (b,c)), is calculated through the following equation:

$$P_{c_a} = \sum_1^{N_c} L_c \tag{14}$$

where N_c and L_c are the number and length of the interface elements in each zone (c) for each interval-angle category (a). It is assumed that, in each square zone, the dominant mesocrack orientation can be either in the primary diagonal direction or in the secondary diagonal direction (see Figure 7 (b,c)). Then, each possible crack path is calculated by adding the P_c zone values in every direction, for each interval-angle category (a), as shown in the Figure 7 (d,e). It is assumed that the best estimation of the tendency of crack development in applications where the damage is shear dominated, can be obtained by adding the P_c in all square sub-zones (diagonal sub-zones) that included in all the possible diagonal paths d as shown in Figure 7 (d,e). Therefore, the possible mesocrack path is calculated for each diagonal d represented in Figure 7 (d,e) by:

Large-scale failure prediction of clay rock using multiscale modelling

$$P_{d_a} = \sum_{c=1}^{\text{num of diagonal sub}-\text{zones}} (P_c)_a \tag{15}$$

Another significant characteristic that triggers the development of mesocracking is the frequency of aligned interface elements which form possible crack paths. Therefore, same values of P_{c_a} (for an interval-angle category (a)) can be gathered in the same diagonal direction (black arrow in Figure 7 (d,e)) and this can be assumed as an indicator for a crack development Thus, the following expression is used to count the frequency of the aligned interface elements:

$$I_{d_a} = \frac{P_{d_a}}{\sigma_{d_a}} \tag{16}$$

where I_{d_a} is the indicator value, P_{d_a} is calculated by the eq. (14), and σ_{d_a} is the standard deviation of the $(P_c)_a$ values in the diagonal sub-zones for each interval-angle category (a).
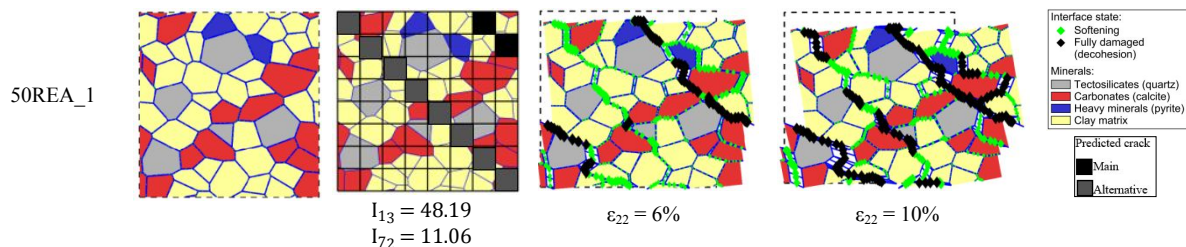
Finally, the proposed strategy can be summarised with the following steps:
1. Calculate the indicator value I_{d_a} for all each diagonal direction for both primary and secondary diagonal orientations.
2. Find the max for each primary / secondary diagonal orientation.
3. The expected dominant mesocrack path (between the two) is the one with the larger I_{d_a}.

The proposed algorithm can be validated by observing the mesocracking pattern that develops across a REA, after being subjected to a biaxial compression, and by calculating its homogenised shear strain ε_{12} . A positive shear strain $\varepsilon_{12} > 0$ can lead to shear cracking in the primary diagonal direction while a negative shear strain $\varepsilon_{12} < 0$ can lead to shear cracking in the secondary diagonal direction (Figure 7 (b,c)). Note, however, that this morphological analysis ignores the periodic condition that constrain the mesocracking of the REA.

5.1.3. **Validation**

In order to validate the mesocrack-prediction strategy, the deformation of several REAs are examined under a biaxial compression condition. Eight REAs with the same material characteristics (see Table 1) are examined in this section. The structure of each REA with its mineralogical distribution, is shown in Figure 8 (a). The study includes REAs with different number of cells, 50, 100, and 250, corresponding to different sizes, L_{REA} = 50, 70, and 105 μm, with the largest mesostructures being more representative of the rock mesostructure [16,44]. As it can be seen in Figure 8 (a), 5 REAs with 50 numerical cells (50REA_1-5), 1 REA with 100 cells (100REA_1), and 2 REAs with 250 cells (250REA_1-2) are studied. According to the proposed strategy, the P_{d_a} and I_{d_a} variable are calculated for both directions (primary and secondary). The mesostructures used in this paper are selected after an analysis of many REAs having variable mineral arrangements (see in Pardoen et al.[16]). The chosen (REAs) have a behaviour close to the experimental one.

50REA_1

$I_{13} = 48.19$
$I_{72} = 11.06$

$\varepsilon_{22} = 6\%$

$\varepsilon_{22} = 10\%$

Interface state:
Softening
Fully damaged (decohesion)
Minerals:
Tectosilicates (quartz)
Carbonates (calcite)
Heavy minerals (pyrite)
Clay matrix
Predicted crack
Main
Alternative

12

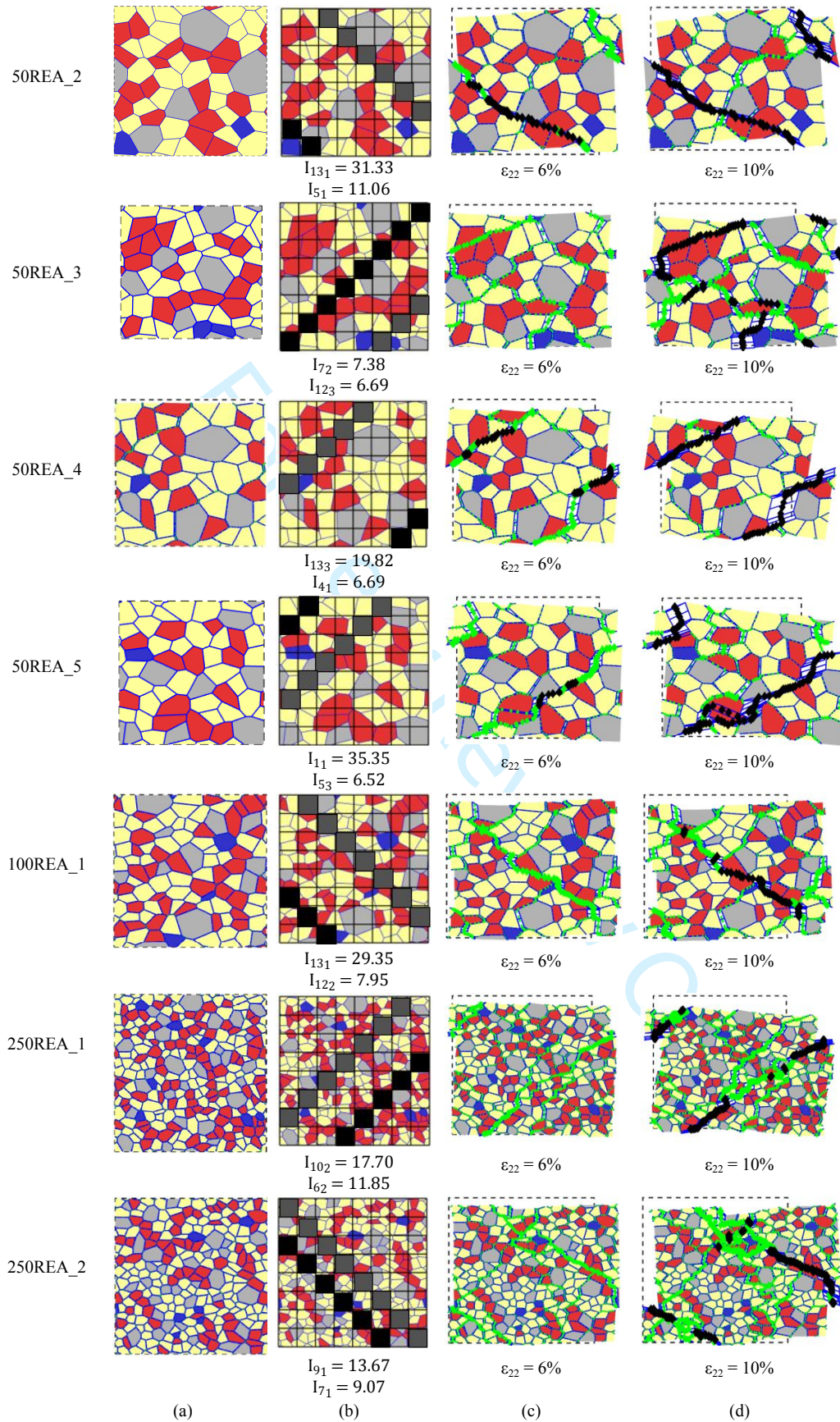*Large-scale failure prediction of clay rock using multiscale modelling*

Figure 8. Mesocracking prediction: (a) structure of selected REAs used for validation, (b) possible mesocrack paths development according to the prediction indicator values, and (c-d) mesorack patterns developing in REAs under biaxial compression.

13

Large-scale failure prediction of clay rock using multiscale modelling

1   The schematic representation of the possible mesocrack paths with the corresponding prediction
2 indicators are shown in the Figure 8 (b). For the 50REA_1 and 50REA_2, the largest value of the I_{da} is
3 found for a=3[45°-67.5°], d=1 (see Figure 7 (d,e)), and a=1[0°-22.5°], d=13, respectively, in the primary
4 direction. The values of the prediction indicators are calculated as $I_{13} = 48.19$ (50REA_1) and $I_{13_1} =$
5 31.33 (50REA_2), respectively. On the contrary, the three others 50cell-REAs present a possible
6 mesocrack path in the secondary direction with values of $I_{72} = 7.38$ (50REA_3), $I_{13_3} = 19.82$
7 (50REA_4), and $I_{11} = 35.35$ (50REA_5), respectively. It has to be noted that, the proposed strategy
8 predicts short mesocrack paths in some cases (50REA_1, 50REA_2, 50REA_5). However, the method
9 indicates a tendency which probably corresponds to the first (main-) dominant mesocracks that are going
10 to develop during the deviatoric-shear loading. The second longest mesocrack path is also displayed in
11 Figure 8 (b) as the second (alternative-) dominant direction for each REA. In this way, it is easier to
12 compare the predictive capabilities of the proposed method with the mesocrack paths that develop in the
13 material under loading (derived from the numerical analysis). Additionally, the REA with 100 cells
14 (100REA_1) presents a tendency to develop a shear strain concentration in the primary direction with a
15 value of $I_{13_1} = 29.35$. Finally, for the more representative REAs with 250 cells, the highest value of I_{da}
16 is found for 250REA_1 in the secondary direction (with a value of $I_{102} = 17.70$), while for 250REA_2
17 it was found in the primary direction (with the value of $I_{9_1} = 13.67$).

18   To validate the above predictions made from the geometry of the mesostructure, the
19 development of mesocrack patterns and the evolution of homogenised shear strain of the REA under
20 deviatoric-shear loading are analysed hereafter. The homogenised shear strain of the REA, derived
21 during the biaxial compression modelling, indicates the direction tendency of the strain localisation at
22 macroscale. The evolution of the shear strains ε_{12} versus the imposed vertical strain ε_{22} is illustrated in
23 the Figure 9. The 50REA_3, 50REA_4, 50REA_5, and 250REA_1 present a shear strain with a negative
24 value $\varepsilon_{12} < 0$ (secondary mesocrack direction), while the others present a positive value $\varepsilon_{12} > 0$
25 (primary mesocrack direction). The Figure 7 (b,c) shows the sign convention related to the mesocrack
26 directions in a simple shear case. Therefore, the proposed geometrical indicator for the direction of crack
27 development allows to predict the REA global shearing, as it can be seen in Figure 8 (b) and Figure 9.
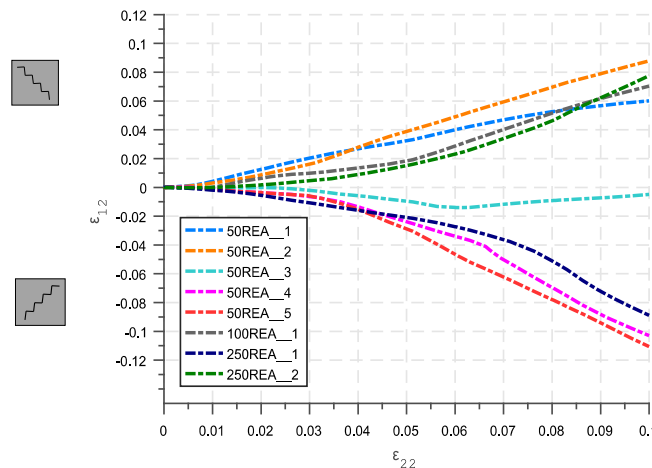

28   *Figure 9. Homogenised shear strain ε_{12} of several REAs under deviatoric-biaxial loading.*

29   The crack patterns of the REAs that are derived from the biaxial compression test, can be seen
30 in Figure 8 (c). As concerned the 50cell-REAs, the dominant crack paths are well predicted for the
31 50REA_1, 50REA_4, and 50REA_5 counting both "main" and "alternative" crack paths (see Figure 8
32 (b)). Furthermore, it can be seen that for the case of the 100REA_1 and 250REA_1 the main diagonal
33 cracks are captured by the "alternative" crack path. As concerned the 250REA_2, the possible crack
34 path (shown in the Figure 8 (b)) is close to the one (the shortest one) of the two main cracks derived
35 from the biaxial analysis. It can be observed that, in many cases, the crack paths change orientation

14

Large-scale failure prediction of clay rock using multiscale modelling

along their length. As it can be seen for the crack patterns of 50REA_2 (see Figure 8 (b)), the largest crack starts with an orientation angle of 50° and ends with an angle near 20°. Finally, it is clear that the 50REA_3 presents a diffused crack pattern. In these cases, the proposed methodology has difficulties to predict the exact position of the dominant mesocrack. However, the tendency of the crack orientation (primary or secondary) is well predicted in all cases.

5.2. Double-scale modelling

The effects of mesocracking on macro-shear banding development in a pluricentimetric rock sample (dimension=5x2.*5cm*) is analysed hereafter. The biaxial compression test is reproduced at larger scale by using the double-scale numerical modelling approach.

5.2.1. Biaxial compression

A schematic representation of the numerical model, the boundary conditions of the macro and meso scales, and the used finite element (FE) meshes are illustrated in Figure 10. An isotropic compression is initially applied on the macro sample and the REAs are initially set as in equilibrium with this confining pressure σ_{11}. In order to do so, the REA is isotropically preloaded with σ_{11} and is imported to the double scale analysis on each Gauss point. The confining pressure that is considered in this study is of $\sigma_{11} = 12\ MPa$. Then, the deviatoric loading is imposed by increasing the macro-vertical strain ε_{22} on the top surface of the sample (with a strain rate of $d\varepsilon_{22}/dt=10^{-10}s^{-1}$). Concerning the hydraulic conditions, the clay rock is considered as fully saturated with water (initial pore water pressure of $p_{w,0} = 0\ MPa$) and the sample is globally drained on the top and bottom surface of the sample (constant $p_w = 0\ MPa$). Hereafter, the macroscale sample is discretised with 20x10 or 40x20 (9-noded) quadrilateral finite elements. It has to be noted that, the value of D is chosen after a numerical investigation, in order to produce mesh-objective results in case of strain localisation. Therefore, for the analysis of these two numerical models, the values of D = 16 N and D = 4 N are used (see 3.1 for definition of D) for the 20x10 and 40x20 models accordingly. The value of D conditions the width of the shear band which is small in clay rocks. Thus, the values of D have been chosen such that the shear band has a small thickness (for both meshes). However, it has been shown that few (at least three) finite elements are required within the band thickness to have a better numerical precision of the post localisation plastic behaviour inside the strain localisation band [45].
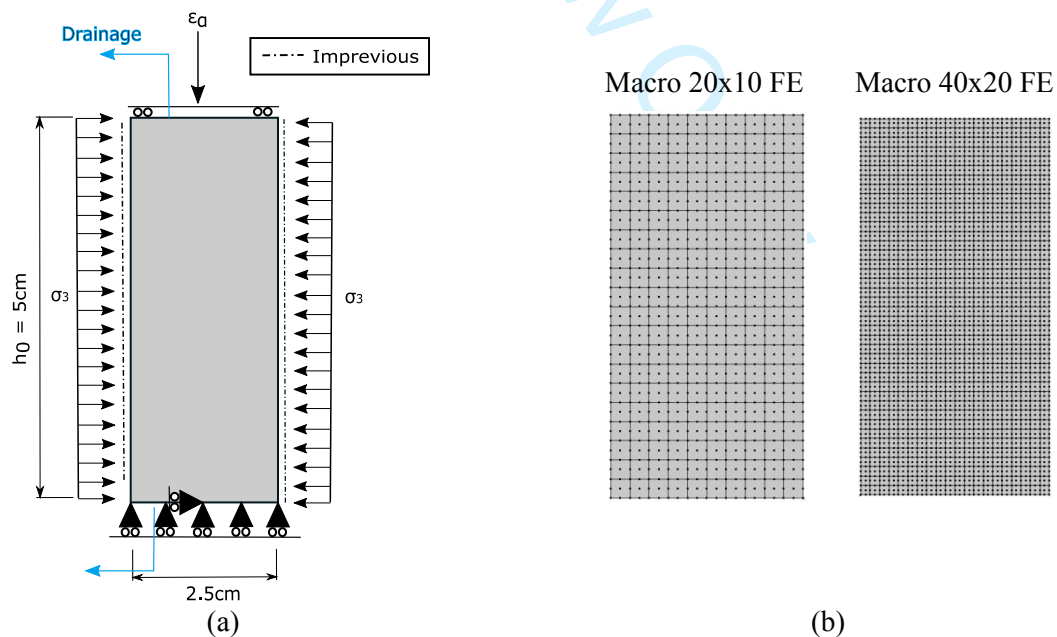

Figure 10. Numerical model of a 2D plane-strain biaxial compression test performed with a double-scale FEM×FEM approach: (a) boundary conditions and (b) meshes.

15

1　　　　The results of the double-scale analysis using the 20x10 discretisation model (see Figure 10),
2　are illustrated in Figure 11. The results are presented in terms of deviatoric stress-vertical strain relations.
3　Additionally, in Figure 11, the numerical results are compared with experimental data derived from
4　triaxial compression tests performed on laboratory specimen of COx clay rock [33,46]. The comparison
5　between numerical and experimental results is important in order to validate the proposed numerical
6　approach, even if the loading conditions are not quite similar. In Figure 11, it can be seen that, the meso-
7　and the double- scale responses are similar until they separate at the onset of strain localisation in the
8　double-scale computations. One can note that the incipient shear bands developing across the sample
9　initiate before the constitutive stress peak (of the mesoscale responses) and induces a strain softening of
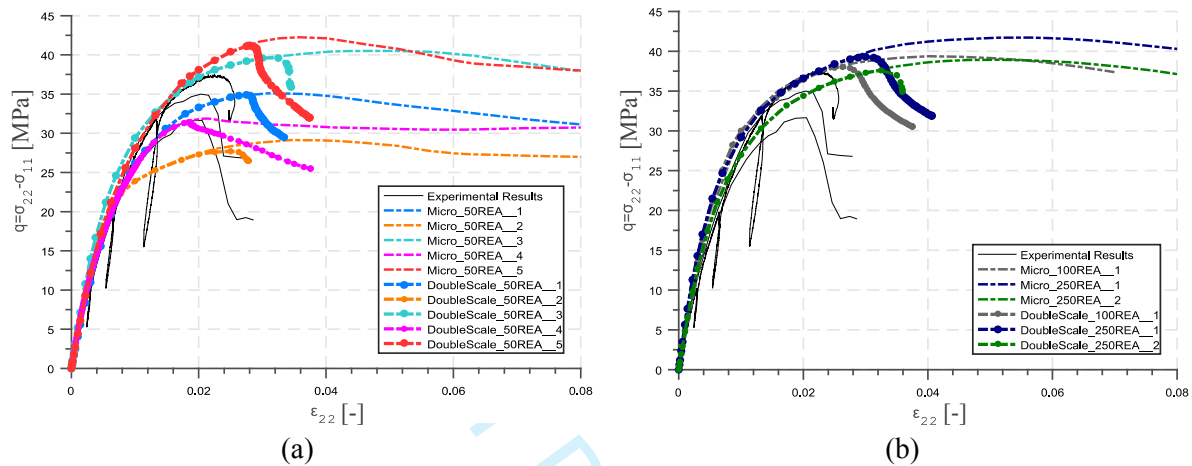10　the double-scale responses.

11　*Figure 11. Comparison of the meso- and double-scale material responses (200 element mesh) under biaxial*
12　*compression with experimental results, for several REAs with: (a) 50 cells (50 μm), (b) 100 and 250 cells (70*
13　*and 105 μm).*

14　　　　The numerical results are also compared with the experimental data in Table 2. The
15　experimental data consist of 3 tests; therefore, average values of these 3 experimental curves are
16　indicated in the Table 2. The initial stiffness is estimated by the Young modulus that corresponds to the
17　vertical strain equal to $\varepsilon_{22} = 0.2\%$. It can be seen that the stiffness is well captured by all the numerical
18　models with an average deviation between the numerical and experimental values to be equal to 12%.
19　Additionally, the shear strength is captured by the numerical models within 13% accuracy margin.
20　However, the modelling slightly overestimates the vertical strain that corresponds to the shear strength
21　value $\varepsilon_{22}^{\text{peak}}$. These REAs were calibrated to have a resilient plastic behaviour with a small strain
22　softening in order to allow shear strain localisation (shear band) at macroscale (in the double-scale
23　analysis) without snapback.

24　*Table 2. Double-scale stiffness and shear strength of selected REAs with comparison to experimental data.*

	$E_{0.2\%}$ (MPa)	q_{max} (MPa)	$\varepsilon_{22}^{\text{peak}}$ (%)	Deviation of E (%)	Deviation of q (%)	Deviation of $\varepsilon_{22}^{\text{peak}}$ (%)
Experimental (Avg.)	4080.70	34.71	2.11			
50REA_1	3837.06	34.93	2.75	-6.0	0.6	30.3
50REA_2	4621.49	27.71	2.50	13.3	-20.2	18.5
50REA_3	4937.01	39.56	3.25	21.0	14.0	54.0
50REA_4	4300.78	31.41	1.84	5.4	-9.5	-12.8
50REA_5	4240.10	41.18	2.81	3.9	18.6	33.2
100REA_1	4717.36	38.03	2.63	15.6	9.6	24.6
250REA_1	5179.61	39.27	3.00	26.9	13.1	42.2
250REA_2	4483.12	37.60	3.25	9.9	8.3	54.0

25

Large-scale failure prediction of clay rock using multiscale modelling

The goal hereafter, is to compare the orientation of the shear bands at macroscale with the orientation of the mesocrack pattern predicted for the biaxial compression test at mesoscale (section 5.1). Therefore, shear band appeared for each examined REA (Figure 12). The figure shows the strain localisation in terms of Von Mises' equivalent deviatoric strain $\varepsilon_{eq} = \sqrt{\frac{2}{3}\hat{\varepsilon}_{ij}\hat{\varepsilon}_{ij}}$, with $\hat{\varepsilon}_{ij}$ being the deviatoric strain tensor $\hat{\varepsilon}_{ij} = \varepsilon_{ij} - \frac{\varepsilon_{kk}}{3}\delta_{ij}$. The results show that the inclination of the shear band matches with the predicted crack orientation in the mesoscale (Figure 8) using the proposed model. It has to be noted that the material is initially homogenous in the macroscale mesh, without imperfection. The anisotropy of the mesostructure, controlled mainly by the grain morphology, is the main factor affecting the shear band inclination at macroscale. However, the solutions obtained, showing a spontaneous strain localisation, should not make us forget that the uniqueness of the solutions is not guaranteed. Even if material anisotropy plays a role in guiding the type of solution [43], it cannot be excluded that other localised solutions are possible [32].
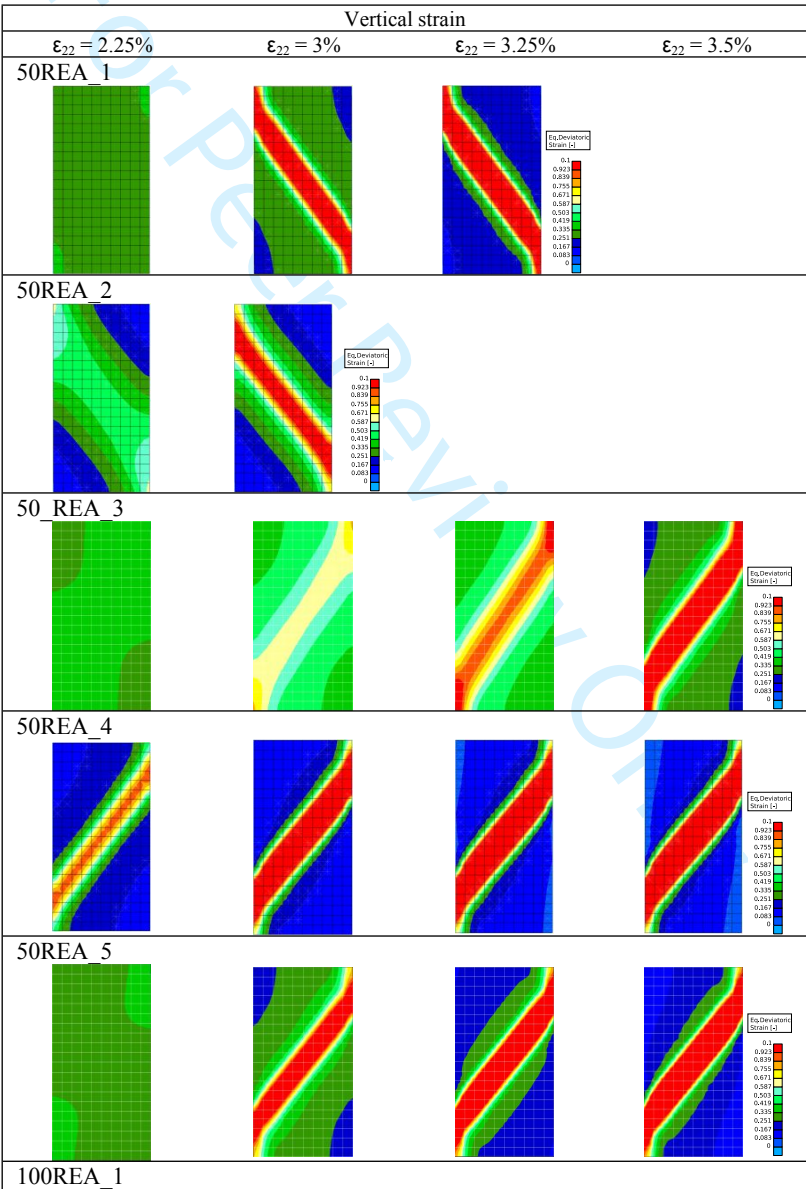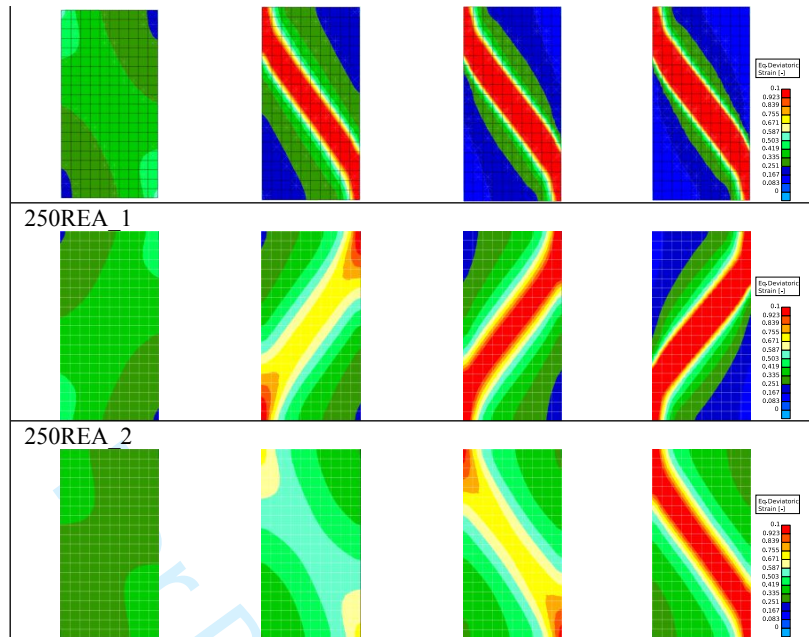
Figure 12. Evolution of equivalent deviatoric strain fields during the biaxial compression test through the double-scale analysis, for several REAs.

Finally, the deformation of each REA in the integration points, inside and outside the shear band, is also presented in Figure 13 for the cases of the 50REA_1 and 50REA_5. Evidently, the orientation of the mesocrack paths corresponds to the same orientation as the one that it is predicted previously with the proposed strategy (section 5.1).

It should be noted that although the overall vertical strain of the sample (macroscale model) reaches the value of 3.25%, the strain is not homogeneous in the sample and is concentrated inside the shear band. Thus, the deformation of the corresponding REAs is (3 times) larger inside the shear band.

(a) 50REA_1

(b) 50REA_5
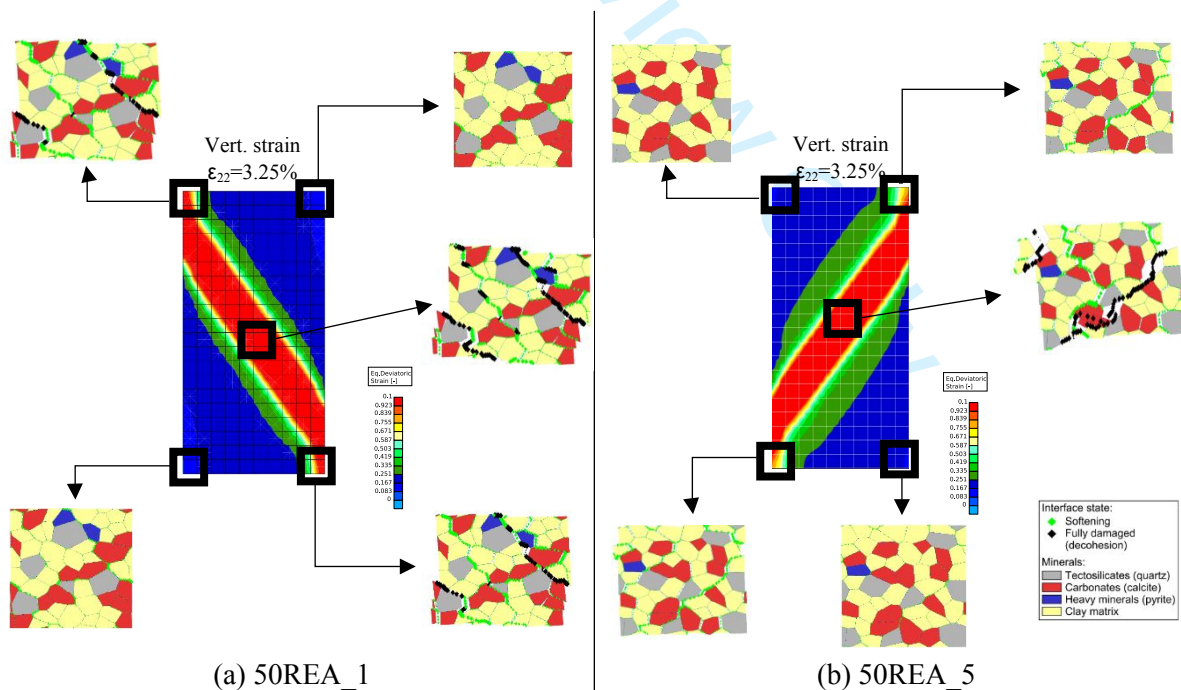
Figure 13. Equivalent deviatoric strain fields and deformed configuration of the REAs, inside and outside the shear band, for two mesostructures: (a) 50REA_1 and (b) 50REA_5.

Finally, the water pressure at ε_{22}=3.25% of overall vertical strain is illustrated in Figure 14. It can be seen that a very small negative water pressure develops within the strain localisation zone.

18

Large-scale failure prediction of clay rock using multiscale modelling

Additionally, the values of the major (maximum) homogenised hydraulic permeability k_{max} of different REAs are indicated in Figure 14. These permeabilities evolve due to deformation and crack developments, as the interfaces between minerals open. The initial permeability of the undeformed material (by defining a minimum hydraulic interface opening) in this study is 1.0e^{-17} m^2. It can be seen that, the value of the major liquid water permeability has a greater value in the center of the specimen, about twice as large, where the REAs are damaged and cracked in the shear band.

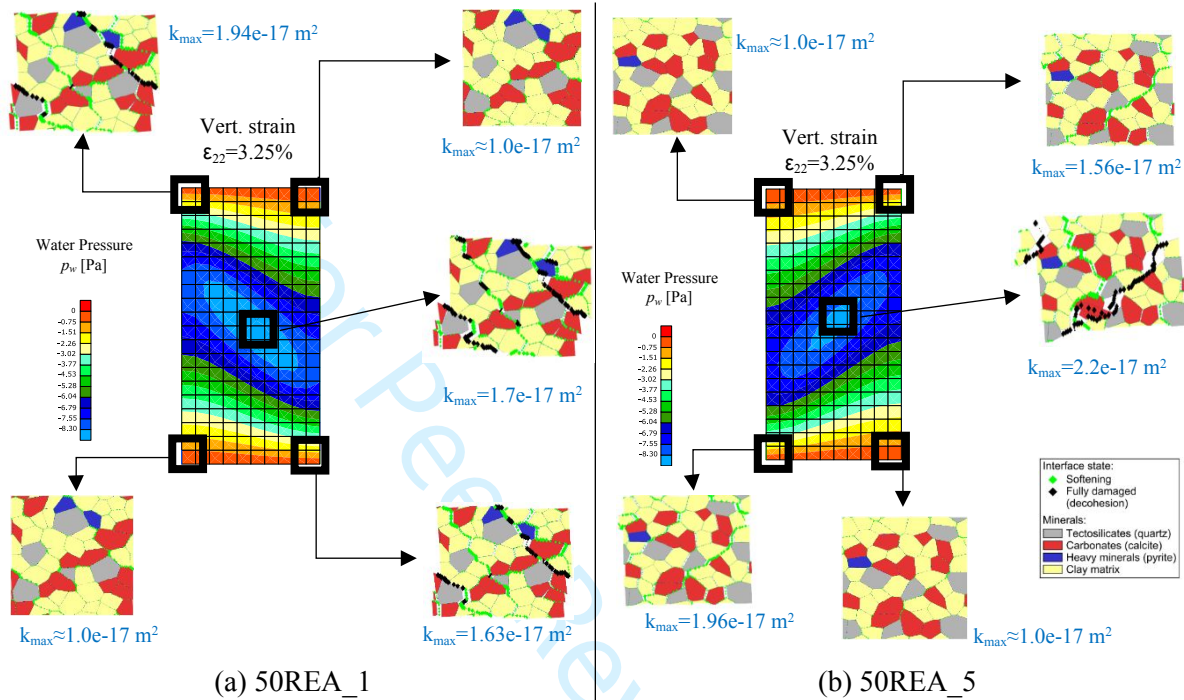(a) 50REA_1   (b) 50REA_5

Figure 14. Water pressure and deformed configuration of the REAs, inside and outside the shear band, for two mesostructures: (a) 50REA_1 and (b) 50REA_5.

5.2.2. Investigation of dominant shear band orientation

The purpose of this study is to examine the shear band orientation as derived from REAs with opposite mesocracking orientation tendencies. The REAs present different material mechanical responses in terms of stiffness, shear strength, and deformability. In this way, this study is going to reveal the material mesoscale characteristic of the REA that triggers the development of one of the two diagonal orientations of the shear band. The latter orientation corresponds with the respective mesocracking tendency of the REA located inside the shear band. Finally, a case study between one REA and its "mirror" configuration is also examined in order to use REAs with the same mechanical response. In this way, the only parameter that affects the orientation of the shear band is the distribution of the REAs and their opposite mesocracking tendencies and anisotropy.

5.2.2.1. *Theoretical and random macro-variabilities*

Three cases are studied in order to examine the different shear band orientations that develop by using REAs with different crack path orientations in the mesoscale. Two REAs are selected for this study: 50REA_1 and 50REA_5. These two REAs present opposite crack path (mesoscale) and shear band (macroscale) inclinations. Furthermore, it can be seen from the Table 2 that the macro (double) scale response with the 50REA_5 presents a stiffer behaviour with a Young modulus 10.5% larger and a shear strength 17.9% larger than the respective properties of the macro-model with 50REA_1. Furthermore, the model with 50REA_5 reaches its stress peak earlier than the model with 50REA_1, as

the vertical strain ε_{22}^{peak} that corresponds to the stress peak is greater by 2.2% than the one of the 50REA_5.

A schematic representation of the macroscale spatial variability of REA for the three cases is illustrated in the Figure 15. It shows a (a) random, (b) horizontal, and (c) vertical distribution of the 50REA_1 (50% in proportion) and 50REA_5 (50% in proportion). These REAs are considered as "weak" and "strong" REA respectively, for the aforementioned reasons, in this study. Furthermore, the biaxial compression test of a macroscale rock sample is conducted for these models and a discretisation of 40x20 finite elements is used as described in Figure 10 (b).

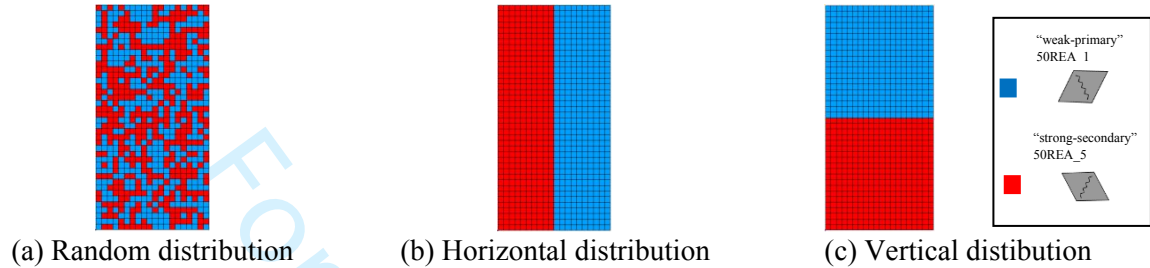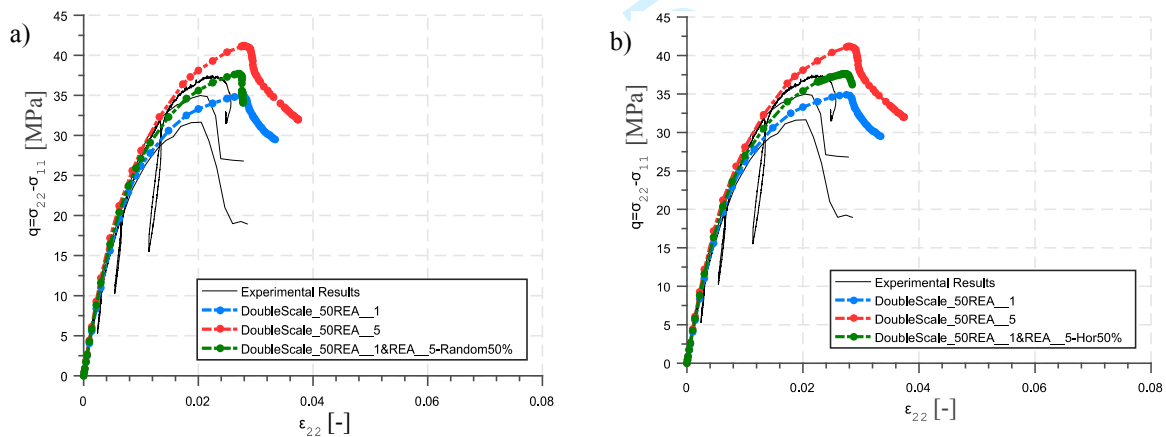| (a) Random distribution	(b) Horizontal distribution	(c) Vertical distibution

Figure 15. Dominant shear band orientation for 50REA_1 and 50REA_5 mesostructures (equally in proportion) with: (a) random, (b) horizontal, and (c) vertical distributions.

The results of the double-scale analysis of the above cases (Figure 15) are illustrated in Figure 16 in the form of deviatoric stress-vertical strain curves (green curve). In Figure 16, the experimental results and the deviatoric stress-vertical strain curves (q, ε_{22}) derived from the double-scale analysis of the biaxial compression test using only the REA_1 (blue curve) and the REA_5 (red curve) are also plotted. For the first two cases Figure 16 (a,b) the green curves are similar and they are located in the middle of the red and blue curves. This average behaviour (i.e. average mechanical response) is explained by the fact that the model contains 50% of each REA. However, in the third case as shown in Figure 16 (c), the green curve does not correspond to an average behaviour since it is close to the blue curve. The latter corresponds to the model with REA_1 only (blue colour in Figure 15).
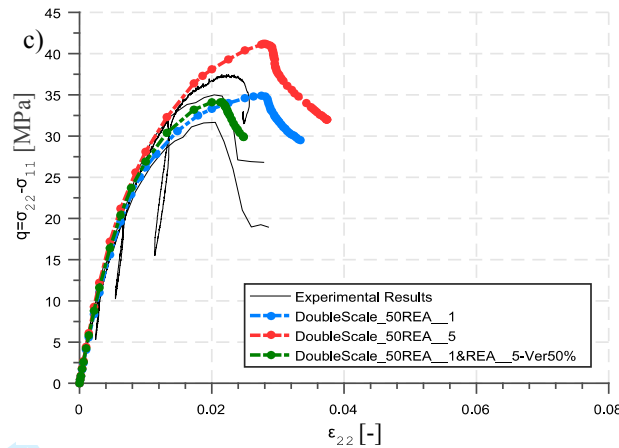
Large-scale failure prediction of clay rock using multiscale modelling

1 *Figure 16. Macro-(double) scale material response under biaxial compression with: (a) random, (b) horizontal,*
2 *and (c) vertical distributions of 50REA_1 and 50REA_5 mesostructures.*

3   The numerical results are also presented in Table 3. It can be seen that all the material response
4 curves show the same stiffness. The first two curves present the same shear strength which is near the
5 average shear strength of the double-scale models with 50REA_1 and 50REA_5 only. The strain that
6 corresponds to stress peak is close to the one with the double-scale model with 50REA_1. Finally, the
7 third case has the lowest shear strength and the material response reaches its peak stress earlier than the
8 others.

9 *Table 3. Macro-(double) scale stiffness and shear strength for: (a) random, (b) horizontal, and (c) vertical*
10 *distributions of 50REA_1 and 50REA_5 mesostructures.*

50REA_1 & 50REA_5	$E_{0.2\%}$ (MPa)	q_{max} (MPa)	ε_{22}^{peak} (%)
(a) Random distr.	4037.01	37.66	2.72
(b) Hor. distr.	4037.26	37.6	2.74
(c) Ver. distr.	4026.92	34.14	2.13

11   Furthermore, in Figure 17, the shear band that develops for each case is illustrated in terms of
12 Von Mises' equivalent deviatoric strain ε_{eq}. It can be seen that, in (b) and (c) cases, the shear band
13 develops firstly in the primary direction in the upper half of the model, in the zone attributed to the
14 "weak" REA. Then this shear band reflects on the top surface due to the imposed vertical displacement
15 (rigid lubricated platen) to form another part with secondary direction. In case (b), the reflected band
16 propagates in the zone attributed to the "strong" REA, while in the (c) case, the shear band is
17 concentrated only in the zone attributed to the "weak" REA. That explains the fact that the overall shear
18 strength of the sample in case (c) is close to the one with 50REA_1 only (see Figure 16 and Table 3).
19 Additionally, the most active part of the shear band (i.e. with larger equivalent deviatoric strain ε_{eq}) is
20 the one with the primary direction because it develops first. This direction is both the direction of the
21 shear band at macroscale and of the crack path in mesoscale of the REA_1. It is obvious that the macro
22 shear failure starts in the location of the REA_1 as it presents a lower shear strength than REA_5 which
23 is reached earlier (see Table 3 and Figure 11 (a-b)).

24   For case (a) (random distribution), the localisation process is more complex (Figure 17 (a)).
25 Well before the peak stress of the macroscopic response (ε_{22}=2.25%), a dense network of parallel and
26 conjugate bands can be distinguished, showing that both primary and secondary orientations are
27 represented. As the stress peak is approached (ε_{22}=2.78%), a main band emerges, which is inclined in
28 the secondary orientation and rapidly induces a softening of the macroscopic response. In this case, the
29 development of macroscale shear banding is affected by the random distribution of the REAs. The
30 difference in stiffness and shear strength between the two REAs triggers the strain localisation. The
31 Figure 17 (last column) shows that the concentration of the "weak" REA_1 (blue colour) attracts the
32 strain localisation. Therefore, having a competition between two REAs, the one that has the less strength

21

Large-scale failure prediction of clay rock using multiscale modelling

1　and stiffness develops more damage than the other during the biaxial compression. The shear band
2　eventually forms by connecting the strain concentrations and it is formed in the secondary diagonal
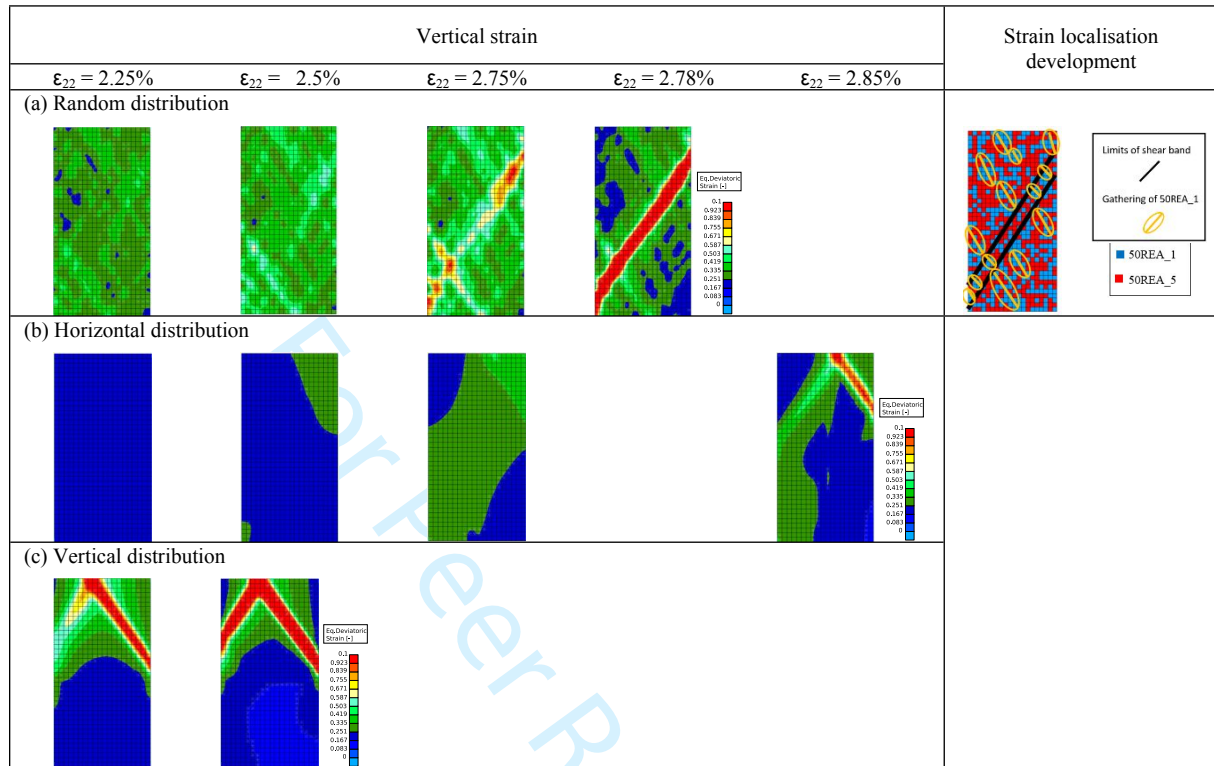3　direction.

4　*Figure 17. Evolution of equivalent deviatoric strain fields during the biaxial compression test through the*
5　*double-scale analysis for: (a) random, (b) horizontal, and (c) vertical distributions of 50REA_1 and 50REA_5*
6　*mesostructures.*

7　　　*5.2.2.2.* Investigation of dominant shear band orientation *between different REAs*

8　　　　In order to thoroughly examine the shear band orientation which develops when using different
9　REAs with different characteristics and material mechanical responses, several case studies are
10　performed with the same binary distribution (blue and red REA location as in Figure 15). The Figure 18
11　illustrates the shear bands (in terms of equivalent deviatoric strains $\boldsymbol{\varepsilon_{eq}}$) which develop, in a COx clay
12　rock sample under biaxial loading, using different REAs. It is interesting to see that different mechanical
13　characteristics of the REAs can lead to different shear bands with different length, shape, and orientation.
14　It is also noted that the strain localisation in the case of a random distribution is in the form of multiple
15　bands that appear before the stress peak of the sample response, and then these bands cease to be active
16　so that a single band takes over the others at the stress peak [43,47,48]. Note that a similar localisation
17　process, with early multiple localisations and then localisation on a single band at peak stress, has been
18　observed experimentally. It has been observed using full field measurements in the COx claystone under
19　some specific loading conditions [48], as well as in a porous sandstone [47].

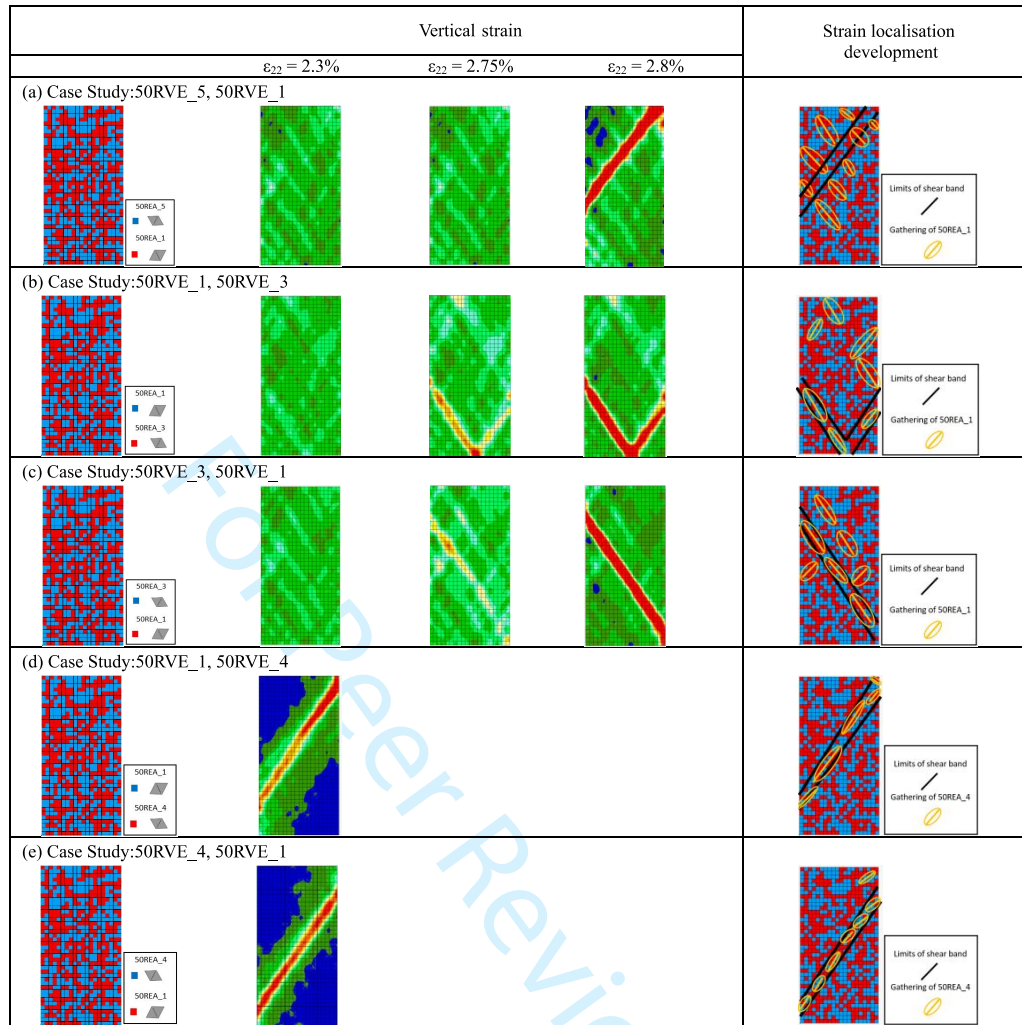*Large-scale failure prediction of clay rock using multiscale modelling*

Figure 18. Evolution of equivalent deviatoric strain fields during the biaxial compression test for several mesostructures and concentration of REAs inside the developed shear bands.

If the REA_5 and REA_1 exchange position, a shear band with smaller length appears but in the same orientation (Figure 17 (a) and Figure 18 (a)). In both cases, (Figure 17-last column and Figure 18), the strain localisations start to form in the location of the 50REA_1 which has a lower stiffness and a lower shear strength. Therefore, when the sample response is close to reach its maximal deviatoric stress and develop a softening behaviour, the strain localisations have an orientation mainly in the primary direction (see Figure 17 (a) and Figure 18 (a) for a vertical strain ε_{22}=2.75%). This primary orientation corresponds also to the predicted cracking orientation of the 50REA_1 in the mesoscale. It can be seen, that these shear localisations are surrounded by elements which are consisted by 50REA_5. In the interaction between these elements and the shear localisations, the elements with 50REA_1 concentrates a largest amount of deviatoric strains. This is explained by the fact that the 50REA_1 has a lower shear strength than the 50REA_5. Eventually, these shear strain concentrations are gathered in the secondary diagonal direction. It has to be noted that, the two REAs do not present severe difference in the strain that corresponds to their shear strength $\varepsilon_{22}^{\mathrm{peak}}$. This is indicated by the fact that inside the shear band there are both elements with REA_1 and REA_5 (see Figure 18 (a)-last column).

For the second case study, the REA_3 has a larger stiffness and shear strength than the REA_1 (Figure 18 (b,c)). Furthermore, the REA_1 reaches its shear strength significantly earlier than the REA_3 (see Figure 11). Therefore, every domain with elements of REA_1 is more vulnerable and accumulates more deviatoric strain. It is obvious that the strain localisations are mainly in the primary diagonal direction, as it is predicted by the mesoscale behaviour of REA_1 (see Figure 18 (b,c)). Due to

23

Large-scale failure prediction of clay rock using multiscale modelling

the random distribution of the two REAs, these shear bands develop in the areas where clearest paths of elements with 50REA_1 are gathered without many elements with REA_3 (see Figure 18 (b,c)-last column). The difference between this case study with the previous (between 50REA_1 and 50REA_5) is that the 50REA_1 reaches its shear strength (and then its post peak softening behaviour) significantly earlier than the 50REA_3. Thus, the elements with 50REA_1 trigger the shear band development.

Finally, the last couple of REAs, REA_1 and REA_4 (Figure 18 (d,e)), presents a similar shape and orientation of shear bands as for the case study of REA_1 and REA_5. This means that the predicted mesocrack orientation of the REA_4 prevails. However, in this case the strain localisations start to appear mainly in the secondary diagonal orientation. The REA_4 is weaker than the REA_1 in terms of shear strength and it reaches it under less deformation than the REA_1 (see Figure 11). This leads to a shear band development in the secondary direction. Furthermore, the strain localisations start at both lateral sample faces (right and left) in some areas where elements with REA_4 gather. Then these strain localisations connect in a shear band, following the secondary diagonal direction (see Figure 18 (d,e)-last column).

5.2.2.3. *Mirror mesostructure*

In this subsection, a case study is conducted using the REA_1 and its symmetric REA with the vertical axis being the axis of symmetry (horizontal flip of the REA), as illustrated in Figure 19. This REA is called as "mirror" REA and the REAs have the same mechanical response with a reverse anisotropy. Therefore, the shear band orientation is affected only by the mesocracking tendency (anisotropy) and distribution of the REAs in the macroscale rock sample.
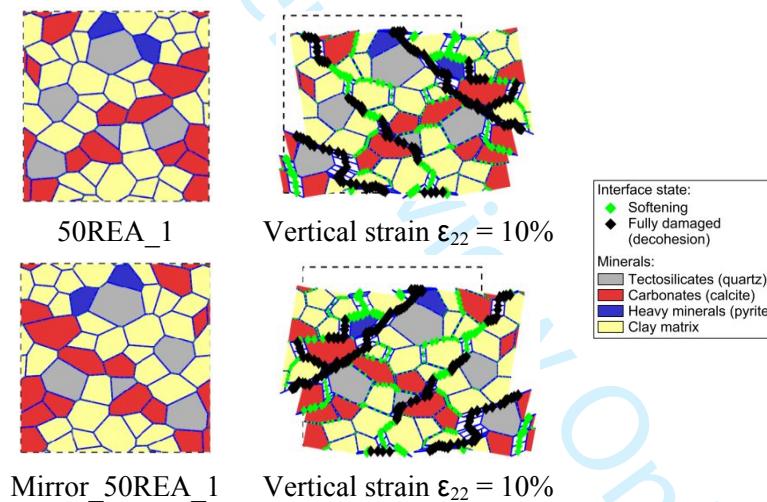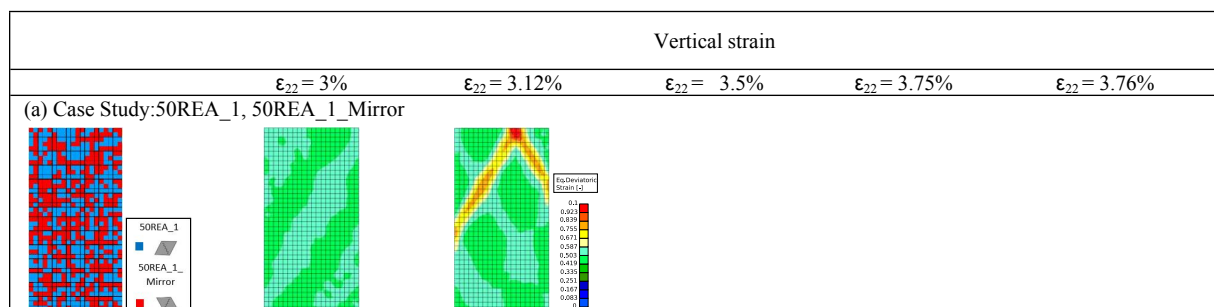

50REA_1	Vertical strain ε_{22} = 10%
Mirror_50REA_1	Vertical strain ε_{22} = 10%

Interface state:
◆ Softening
◆ Fully damaged (decohesion)

Minerals:
■ Tectosilicates (quartz)
■ Carbonates (calcite)
■ Heavy minerals (pyrite)
□ Clay matrix

Figure 19. Structure of the 50REA_1 and mirror 50REA_1 as well as their deformed and damaged states.

As expected, the two REAs present the same mesocrack paths but with opposite orientations. In fact, both REAs present the same damage state by decohesion (black zones) and the same deviatoric stress-vertical strain response. The Figure 20, shows the shear band development in rock samples under biaxial loading (i.e. the evolution of the equivalent deviatoric strain ε_{eq}) using REA_1 and "mirror" REA_1.

Vertical strain				
ε_{22} = 3%	ε_{22} = 3.12%	ε_{22} = 3.5%	ε_{22} = 3.75%	ε_{22} = 3.76%

(a) Case Study:50REA_1, 50REA_1_Mirror

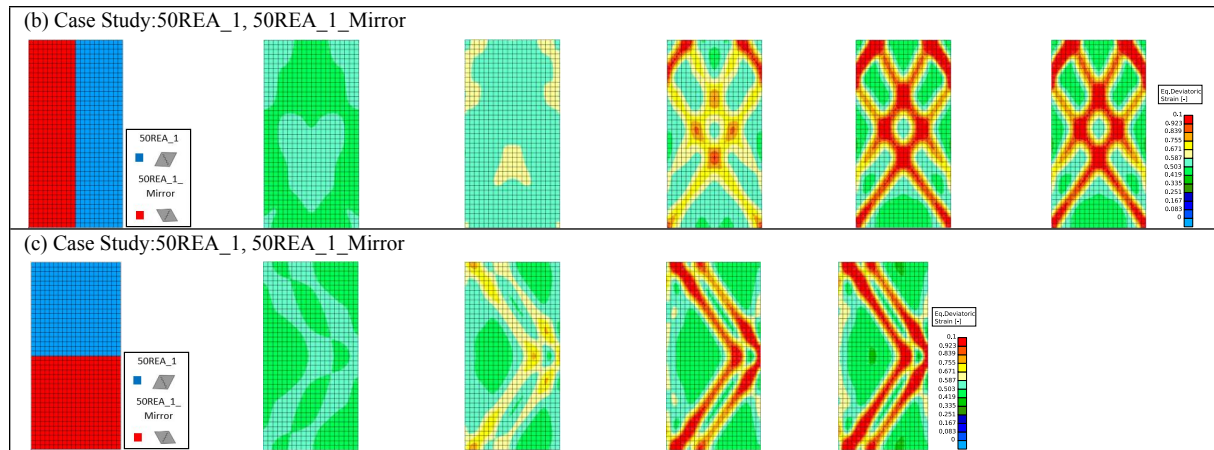*Large-scale failure prediction of clay rock using multiscale modelling*

Figure 20. Evolution of equivalent deviatoric strain fields during the biaxial compression test for the case studies where 50REA_1 and mirror 50REA_1 mesostructures are used.

In the first case study (random REA distribution, Figure 20 (a)), it can be seen that when the vertical strain is 3%, the deviatoric strains are concentrated in the secondary direction. However, when vertical strain is equal to 3.12%, it can be seen that the largest deviatoric strains are gathered in the top of the model, in the area where mainly 50REA_1 is concentrated. From this concentration, it can be assumed that the shear band develops in the primary direction firstly and then it reflects on the top sample face in the secondary direction. It has to be noted that the shear band in the primary direction includes mainly 50REA_1 (blue colour in Figure 20 (a)), while in the secondary direction there are mainly 50REA_1_mirror (red colour in Figure 20 (a)). Note that in this case of random distribution, there is no preliminary localisation before stress peak, due to the exact equality of the strength between the two REA.

In the second and third cases (horizontal and vertical REA distributions, Figure 20 (b,c)), it is clear that the shear bands are formed according to the REA distribution and they have the orientation following the mesocrack path tendency of each REA. For the second case (Figure 20 (b)), the shear bands reflect on the top and the lateral sample faces, creating shear bands in both orientations around the central (vertical) axis of symmetry. As concerned the third case (Figure 20 (c)), it is evident that the shear band orientations agree with the mesocracking tendencies.

6. *Mesoscale effects on excavation damaged zone modelling*

The large-scale fractures that are developed around underground structures, induced by their excavation, are modelled in this section. The large-scale shear fracture process in the EDZ is numerically represented by strain localisation in shear bands [49]. The double-scale approach is used to simulate the boundary value problem representing the gallery excavation in two-dimensional plane strain conditions. In this section, to investigate the effect of the REA on the excavation damage zone (EDZ) development, several REAs are tested, which correspond to different shear band orientations in the biaxial compression test. Two preliminary remarks must be made. Firstly, the loading paths that will be followed in the vicinity of the gallery wall are far from the biaxial compression type loading conditions discussed earlier. As the mode of mesofissure coalescence is dependent on the type of loading, the damage patterns at the mesoscopic scale will be very different from what has been shown above. Therefore, the notion of primary or secondary damage orientation, which was presented on a biaxial compression path, is not as relevant here. However, for reasons of consistency with the presentation of the previous paragraph, we continue to retain this distinction which refers to different anisotropies of the mesostructure. Moreover, a limitation of the model in its current version is that it can only increase the pore volume occupied by the pore fluid. As a consequence, decreases in pore pressure in the deforming zones, in particular within the localisation bands, are to be expected and probably

25

Large-scale failure prediction of clay rock using multiscale modelling

1 overestimated. However, it is interesting to study what impact the mesostructure has on the strain
2 localisation pattern in the EDZ. This is the subject of this section.

3 ### 6.1. Numerical model

4   The examined gallery corresponds to the GED gallery of Andra's URL oriented parallel to the
5 minor horizontal principal total stress and has a radius of 2.6m. A schematic representation of the model,
6 the meshes, and the boundary conditions is depicted in the Figure 21 (a). The initial stress state in the
7 gallery section is anisotropic with $\sigma_{x,0} = 16.12$ MPa and $\sigma_{y,0} = 12.7$ MPa. The deconfinement curves,
8 that describe the total stress and pore water pressure imposed at the gallery wall, are presented in the
9 Figure 21 (b). Additionally, a conceptual model of the chevron fractures [6,46] is illustrated in the Figure
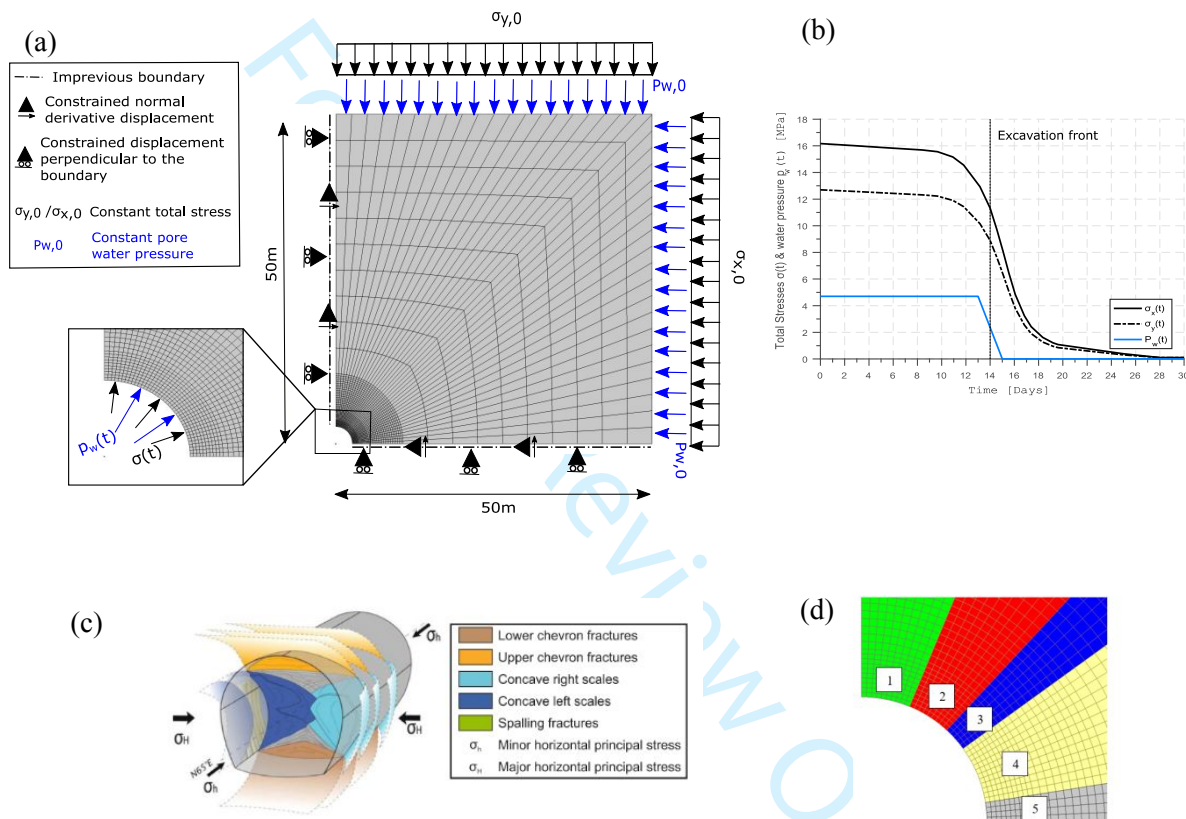10 21 (c) at the front of this gallery.

11 *Figure 21. Schematic representation of the gallery excavation model: (a) mesh and boundary conditions, (b)*
12 *deconfinement curves of the total stresses and pore water pressure at gallery wall, (c) conceptual model of the*
13 *induced fractures in COx clay rock [6,46], and (d) separated areas around the gallery.*

14   A quarter of the gallery is modelled in this study by assuming symmetry along the x and y-axes.
15 The mesh extension is 50 m, both horizontally and vertically and the discretisation is performed with a
16 total of 9801 nodes and 2480 elements. The initial stresses and pore water pressure are imposed at the
17 mesh external boundary (drained boundary) and the mesh has a more refined discretisation close to the
18 gallery. To establish the symmetry, the normal displacements and the normal water flows are blocked
19 to a value of zero along the symmetry axes, which are therefore impervious. Furthermore, an additional
20 kinematic condition is also implemented to establish symmetry in the model considering the gradient
21 terms in the equilibrium equations [50]. Therefore, the radial displacement must be symmetric on both
22 sides of the symmetry axes, which implies that the normal derivative of the radial displacement is null
23 on the symmetry axes. For this numerical analysis, the value of D = 5000 N is chosen (see 3.1 for
24 definition of D). It has to be pointed out that the investigation that is described below, studies the
25 mechanical behaviour of the COx material during the excavation.

26 ### 6.2. Effect of mesostructure with primary crack path orientation

26

Large-scale failure prediction of clay rock using multiscale modelling

For this gallery modelling, the 50REA_1 is used with the same material parameters (see Table 1) that are used in the previous chapters. The evolution of the Von Mises equivalent deviatoric strain ε_{eq} field until the end of the excavation is illustrated in Figure 22. The stress reduction at gallery wall, from the initial stresses $\sigma_{x/y,0}$, is defined by $\sigma_{x/y,wall} = (1-\lambda)\,\sigma_{x/y,0}$ with the deconfinement rate λ which evolves from 0 to 1, following a deconfining curve. At the first unloading stages during the excavation, quasi axisymmetric diffuse strains develop around the gallery. However, close to the end of the excavation, shear bands (representing the shear and mixed fractures) appear with a preferential development in the sub-vertical direction. The latter corresponds to the direction of the minor principal stress σ_v in the gallery section. It is obvious that the stress anisotropy in the gallery section dictates the preferential development of the EDZ above the gallery (see Figure 21 (c)) [49]. There are three areas around the gallery where the deviatoric strains are gathered, two of them close to the top of the gallery and the other one close to the horizontal direction. It can be seen in Figure 22, that the chevron shear fractures (represented by shear bands) develop preferentially in the vertical direction (i.e. in the direction of the minor principal stress in the gallery section) as observed around galleries in the Andra URL [6,46].

t=8.4 days (λ =0.030)   t=14 days (λ =0.300)   t=19.6 days (λ =0.933)

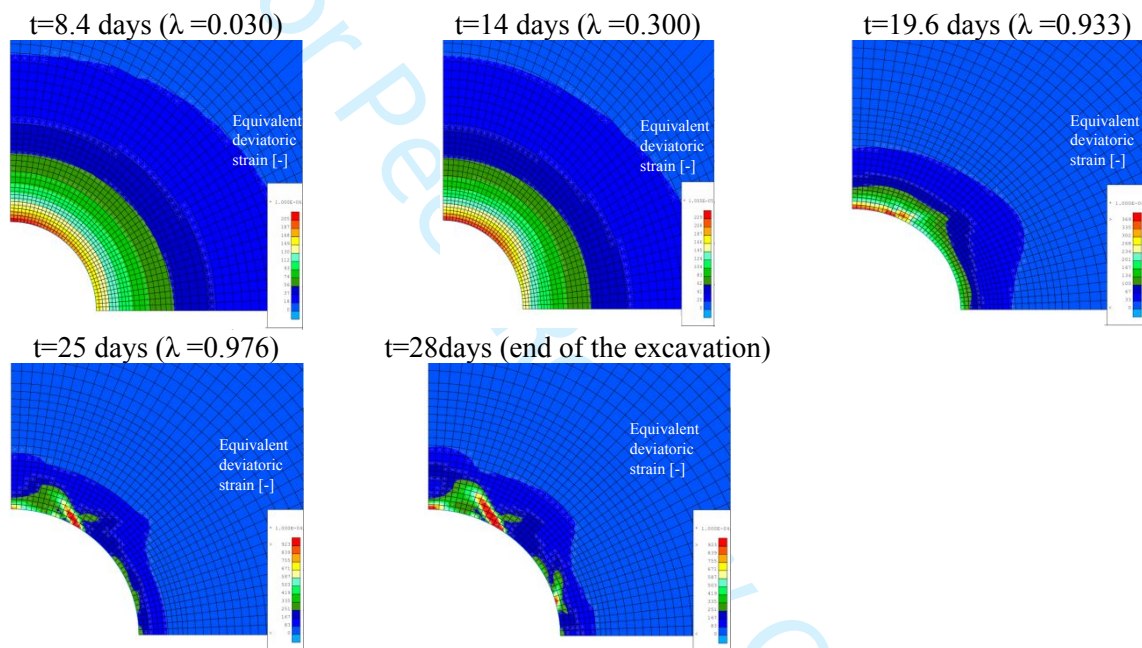t=25 days (λ =0.976)   t=28days (end of the excavation)

Figure 22. Evolution of strain localisation pattern during the gallery excavation using the 50REA_1 mesostructure. The figures correspond to a zoom centred on the gallery.

To further study the developed localisation shear bands, the deformed mesostructures are plotted in different locations (i.e. different integration points) around the gallery at the end of the excavation in Figure 23. It can be observed that different crack patterns in the mesostructure can lead to different shear bands in the macrostructure. The most active shear band contains mesostructures with horizontal mesocracking (area 2-red colour in Figure 21 (d)) while a small strain localisation at the top of the gallery gathers mesostructures with both horizontal and diagonal cracks (area 1-green colour in Figure 21 (d)). It has to be noted that, in the area 2 (red colour in Figure 21 (d)), the REAs present also significant damage in extension (i.e. in the normal direction of mineral contacts). This phenomenon can be explained, considering the loading conditions of the REAs close to the top of the gallery (the orthoradial stress increases while the radial stress decreases at the gallery wall during the excavation) which tend to extend the REAs in the gallery radial direction. Therefore, the modelled EDZ presents mixed-mode fractures (both shear and opening fracture modes) close to the gallery wall which are also observed in the EDZ around galleries of the Andra URL [6,46]. Finally, some strain localisations are present at gallery wall in the horizontal direction (i.e. at the side of the gallery), with shear diagonal mesocracks (area 4-yellow colour in Figure 21 (d)). It has to be pointed out that this cracking direction corresponds with the prediction crack path presented in the previous chapters.
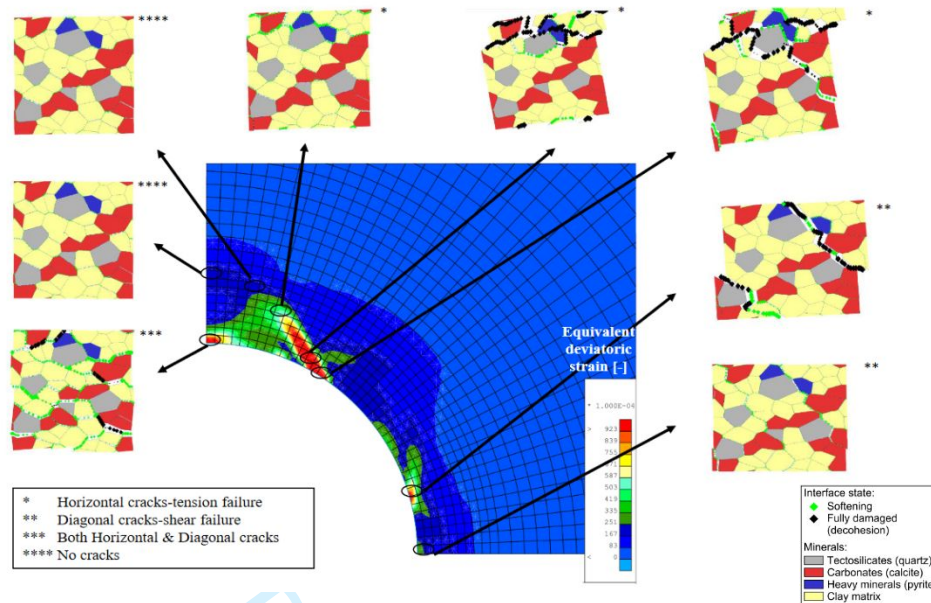
27

Large-scale failure prediction of clay rock using multiscale modelling

1　*Figure 23. Strain localisation at the end of excavation and deformed mesostructures in different locations using*
2　*the 50REA_1 mesostructure.*

3　### *6.3.　Effect of mesostructure with secondary crack path orientation*

4　　　　In order to examine the effect of a different REA with a different tendency of the orientation of
5　the mesocracking in mesoscale and the shear band in biaxial compression test, the 50REA_4 is used for
6　the analysis of gallery excavation. The evolution of the Von Mises equivalent deviatoric strain ε_{eq} until
7　the end of the excavation is illustrated in Figure 24. Similar to previously, it can be seen that in the first
8　unloading stages the deviatoric strains are diffused. However, close to the end of the excavation, the
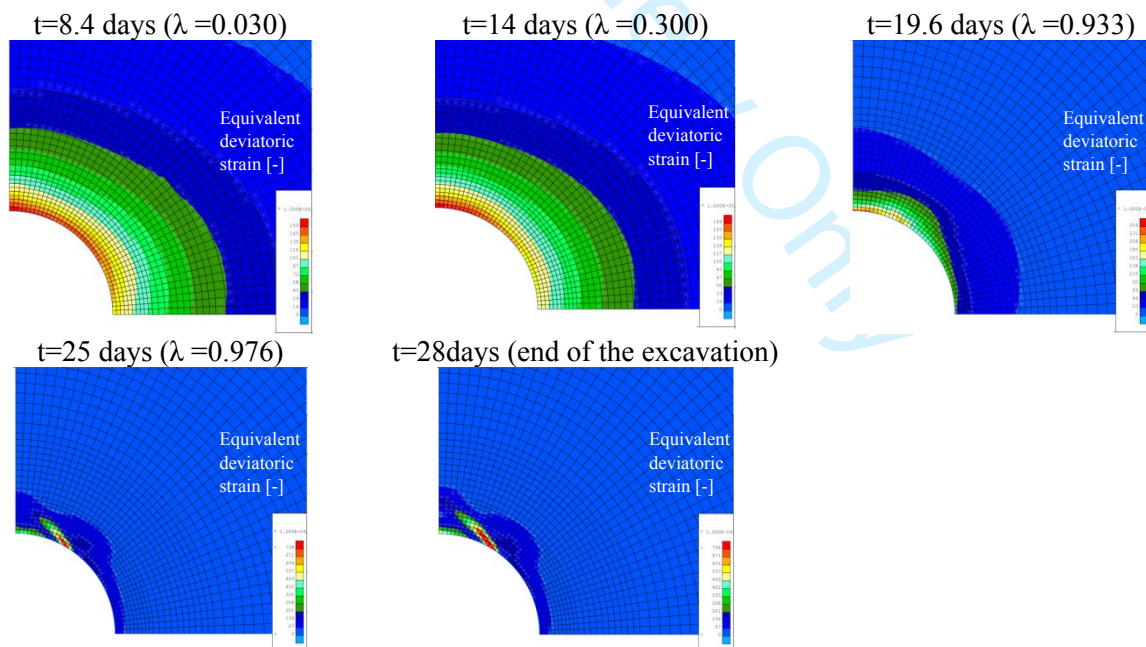9　deviatoric strains are gathered in a small area above the gallery and shear bands develop.

10　*Figure 24. Evolution of strain localisation pattern during the gallery excavation using the 50REA_4*
11　*mesostructure.*

12　　　　The deformed mesostructures in the shear bands are illustrated in Figure 25. It can be seen that,
13　in the largest shear band, the mesostructures develop horizontal mesocracking (area 2-red colour in

28

Large-scale failure prediction of clay rock using multiscale modelling

1 Figure 21 (d); while, at the top of the gallery (area 1-green colour in Figure 21 (d)), the mesostructure
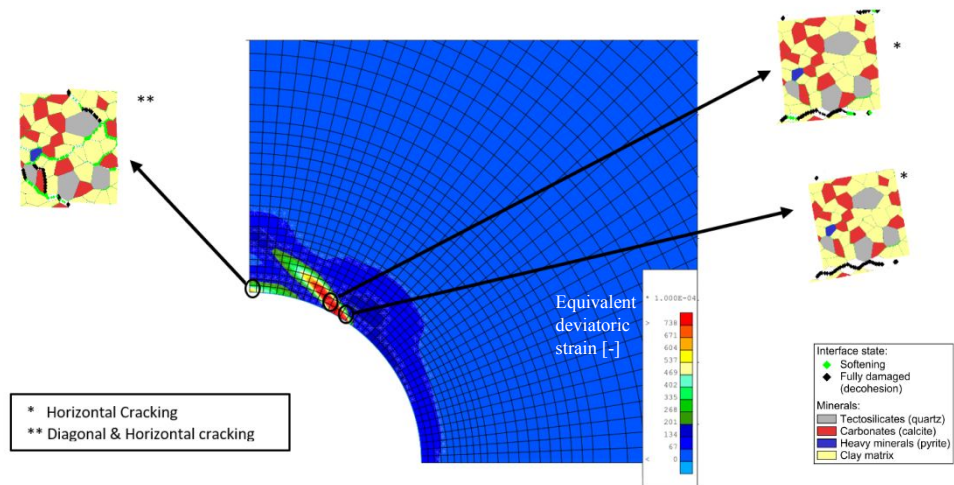2 has both horizontal and diagonal cracking.

3 *Figure 25. Strain localisation at the end of excavation and deformed mesostructures in different locations using the 50REA_4*
4 *mesostructure.*

5   It can also be observed that, compared to the deviatoric strain localisation presented in Figure
6 23, in this case (see Figure 25) no strain localisation develops towards the side of the gallery (area 4-
7 yellow colour and area 5-grey colour in Figure 21 (d)). The mesostructures in this area (see Figure 23)
8 present a clear diagonal cracking similar to the one in the biaxial compression test. Therefore, it can be
9 assumed that, the shear band in this area in the present case (see Figure 25), is deactivated by selecting
10 an REA with the tendency to develop a crack path in the secondary direction.

11   Replacing a mesostructure with another mesostructure, close to each other but with different
12 mesofissure coalescence patterns, induces both similarities and differences in the localisation pattern. In
13 both cases, the dominant main band is quite similar and initiates at approximately the same time, location
14 and orientation. In contrast, other smaller bands may or may not initiate in a dissimilar manner in the
15 gallery wall.

16   **6.4. Random macro-variability of different mesostructures for the gallery excavation**

17   In this subsection, different REAs with different mechanical behaviour characteristics (e.g.
18 shear strength, stiffness) and mesocracking tendencies are randomly distributed in the rock around the
19 gallery. In this way, the characteristics that trigger the development of the shear bands that form the
20 EDZ around the gallery can be examined. Additionally, the random spread of different REAs increases
21 the representativeness of the COx claystone behaviour by taking into account a heterogeneity of the
22 natural material at the macroscale, which would increase the accuracy of the double scale method.

23   **6.4.1. Case study of 2 REAs**

24   In order to investigate the interaction between these two REAs and their effects on shear banding
25 development, they are both used in the same analysis with a random distribution. According to the Table
26 2, the 50REA_4 has a Young modulus 12% larger than the 50REA_1, a shear strength q_{max} 10% lower
27 than the one of 50REA_1, and it reaches its peak deviatoric stress with a vertical strain ε_{22}^{peak} 33% lower
28 than for the 50REA_1 in the biaxial compression test. The random distribution of the two REAs is
29 illustrated in Figure 26.

29

Large-scale failure prediction of clay rock using multiscale modelling

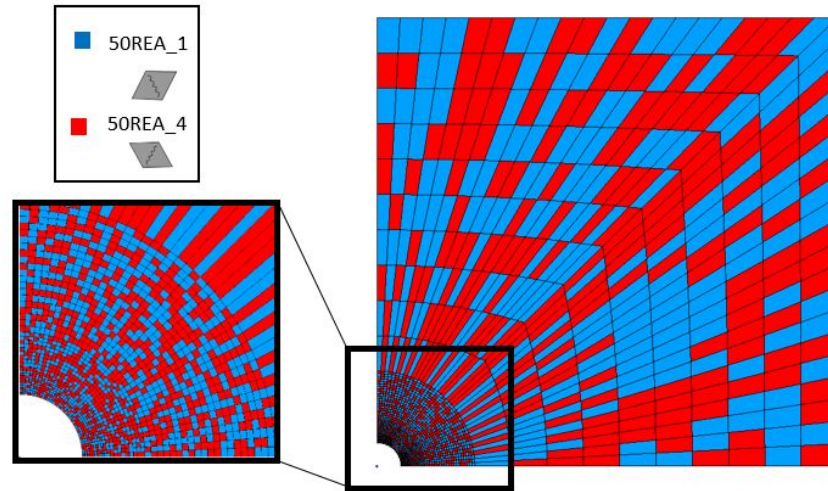1   *Figure 26. Case study for the 50REA_1 and 50REA_4 mesostructures with random distribution (equally in*
2   *proportion).*

3   The evolution of the Von Mises equivalent deviatoric strain ε_{eq} until the end of the excavation
4   is illustrated in Figure 27. Similar to the previous gallery modelling, it can be seen that in the first
5   unloading stages, a quite axisymmetric distribution of the shear deviatoric strains is visible around the
6   gallery. However, it is evident that, due to the difference of stiffness of these two REAs, the deviatoric
7   strain contours present significant fluctuations. Additionally, close to the end of the excavation, the
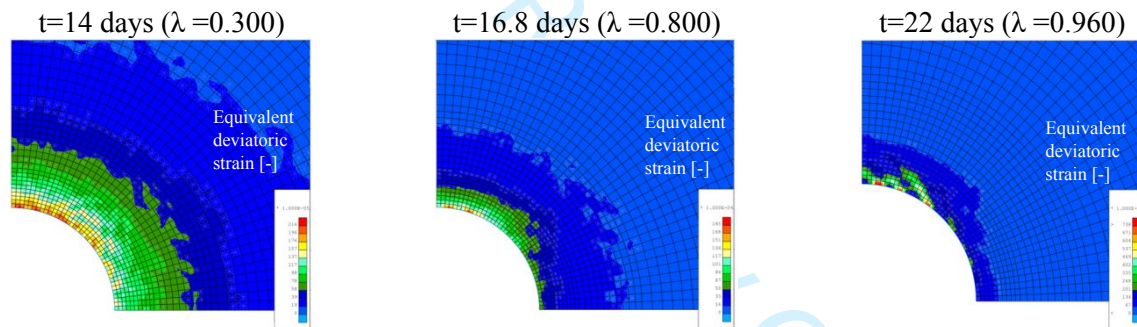8   deviatoric strains are gathered in three small areas near the top of the gallery and shear bands develop.

9   *Figure 27. Evolution of strain localisation pattern during the gallery excavation using the 50REA_1 and 50REA_4*
10   *mesostructures with random distribution (equally in proportion).*

11   The deformed mesostructures in the shear bands are illustrated in Figure 28. It can be seen that
12   the mesostructures 50REA_4 are the ones which gather the shear deviatoric strains and lead to the shear
13   band initiation. Furthermore, the REAs which are above the gallery (area 1-green in Figure 21 (d))
14   present horizontal and diagonal mesocracking while the other shear band (area 2-red colour in Figure
15   21 (d)) contains REAs with horizontal mesocracks. This means that the shear bands are concentrated in
16   the mesostructures REA_4. The most significant factor is, that these mesostructures are reaching their
17   strain softening behaviour earlier than the others. Finally, the area that presents REAs with shear
18   diagonal mesocracking towards the side of the gallery (area 4-yellow colour in Figure 21 (d)) in
19   subsection 6.2 consists of 50REA_4 mesostructure. Therefore, the shear band does not develop in that
20   area, like for the analysis in subsection 6.3, because these REAs have the tendency to develop a
21   mesocrack path in the opposite direction (secondary diagonal).

Large-scale failure prediction of clay rock using multiscale modelling
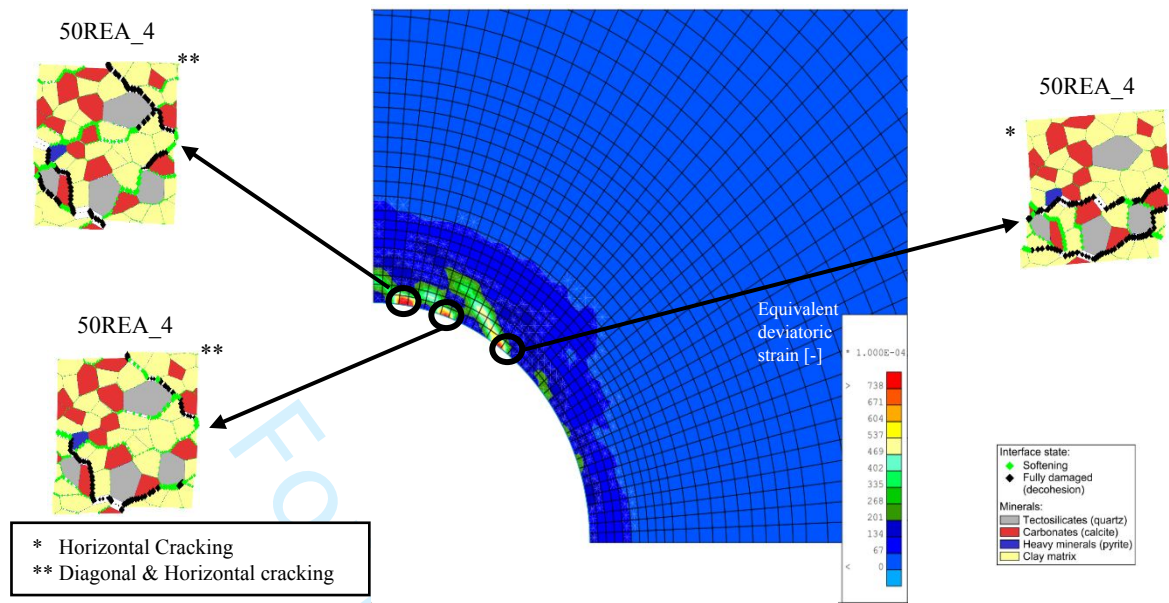

Figure 28. Strain localisation at the 22nd day of excavation and deformed mesostructures in different locations using the 50REA_1 and 50REA_4 mesostructures with random distribution (equally in proportion).

6.4.2. Case study of 4 REAs

In order to investigate further the effect of different damage mechanisms in the mesoscale (of the REA) on the shear band development, four REAs are selected: REA_1, REA_2, REA_4, and REA_5. The random distribution of the 4 REAs are illustrated in Figure 29.
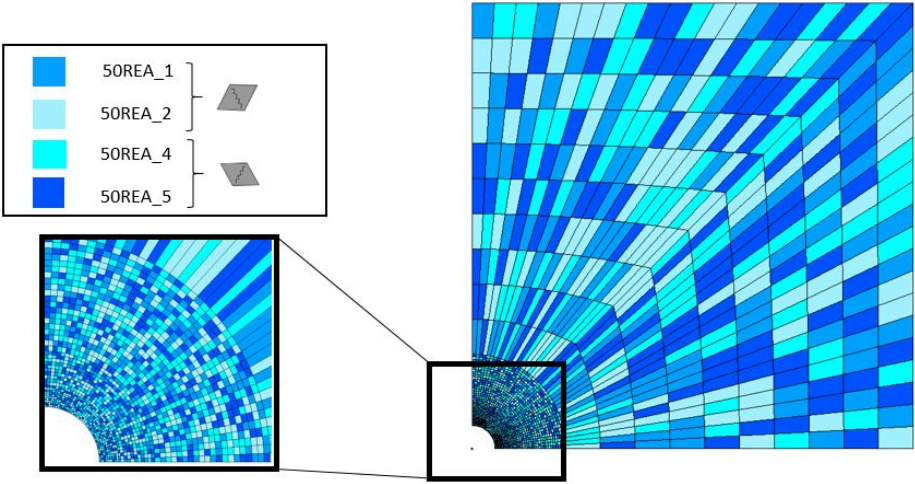

Figure 29. Gallery excavation by using the 50REA_1, 50REA_2, 50REA_4, and 50REA_5 mesostructures with random distribution (equally in proportion).

Two of these REAs (REA_1 and REA_2) have the tendency of mesocracking in the primary diagonal direction while the others have the opposite propensity. The evolution of the Von Mises equivalent deviatoric strain fields until the end of the excavation is illustrated in Figure 30. Similarly to the previous study, the contour of the equivalent deviatoric strain fields present fluctuations even in the first unloading stages. At the end of the excavation, there are severe strain localisations with preferential orientations. The area between the middle and the top of the gallery wall (areas 1, 2, and 3 in Figure 21 (d)) presents shear bands with preferential development in the vertical direction, oriented above the gallery. The strain localisations that appear near the side of the gallery (areas 4 and 5 in Figure 21 (d)) tend to extend both horizontally and vertically downwards.

31

Large-scale failure prediction of clay rock using multiscale modelling

Additionally, a schematic representation of the EDZ as reported experimentally[6,46] is illustrated at the end of the excavation in Figure 30, for comparison. The mixed fracture zone, where both shearing and opening fracture modes appear, extends upwards above the gallery up to 1.2 m, which is close to the experimental measurement (1.27 m). Furthermore, near the side of the gallery, the mixed fracture zone tends to extend horizontally up to 0.4 m, which agrees with the experimental evidence (0.5 m).
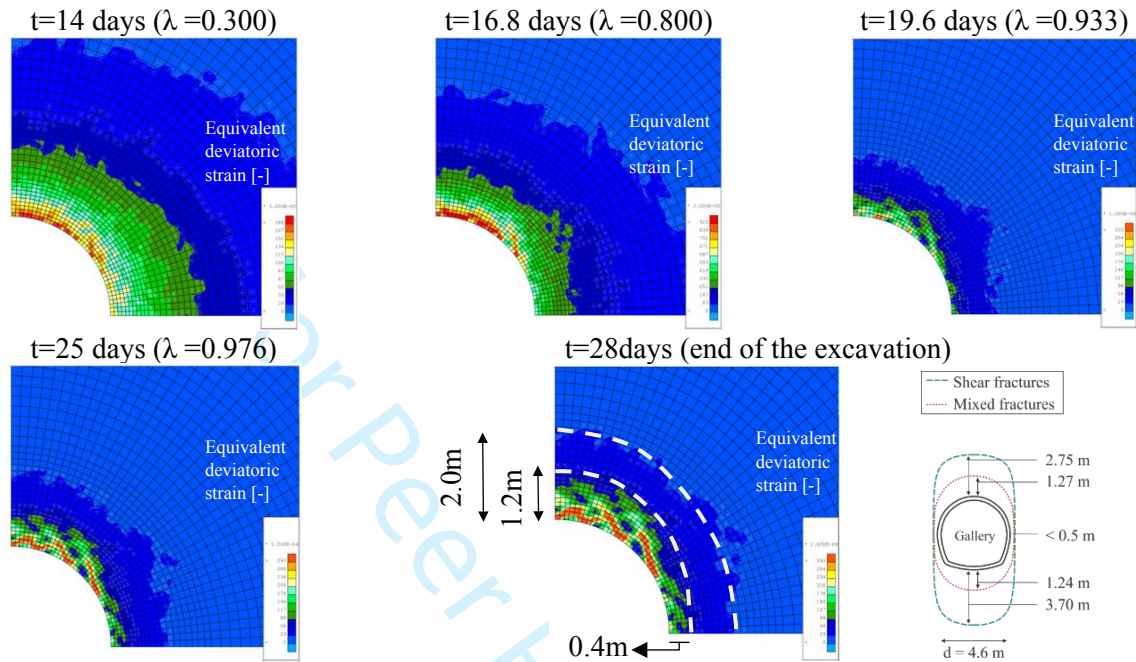

Figure 30. Evolution of strain localisation pattern during the gallery excavation using the 50REA_1, 50REA_2, 50REA_4, and 50REA_5 mesostructures with random distribution (equally in proportion) and comparison with experimental fracture measurements[6,46].

The deformed mesostructures in the shear bands are illustrated in Figure 31. It can be seen that the distribution of stiffness and shear strength through the mesostructures causes the development of severe strain localisations around the gallery. The REA_4 has gathered a severe amount of deviatoric strain, larger than the others. The REA_4 is the REA which has a lower shear strength (see Table 2) than the others. At the side of the gallery (area 5-grey colour in Figure 21 (d)), there is not significant strain localisation. However, there are some concentrations of REA_1 and REA_4 that present diagonal mesocracks in both primary and secondary direction respectively which agree with their mesocrack orientation tendency. On the other hand, close to the middle of the gallery wall (at the top of the area 4-yellow colour in Figure 21 (d), the REA_4 presents horizontal and diagonal mesocracks in both primary and secondary directions. Additionally, the area 2-red colour of the gallery (see Figure 21 (d)) presents REAs with horizontal mesocracking. Finally, above the gallery (area 1-green colour in Figure 21 (d), there are REAs with both horizontal and diagonal mesocracks. The shear bands in this area present opposite directions as illustrated in Figure 31.

It can be seen that the consideration of a heterogeneity in the REA distribution at each Gauss point has a strong impact on both the mode of deformation prior to failure and on the localisation pattern once failure has been initiated. The deformation concentration zones are much more numerous and extensive than in the case of a homogeneous material. The main band observed in the simulations on a homogeneous medium is preserved, but other competing bands of the same magnitude are also observed.

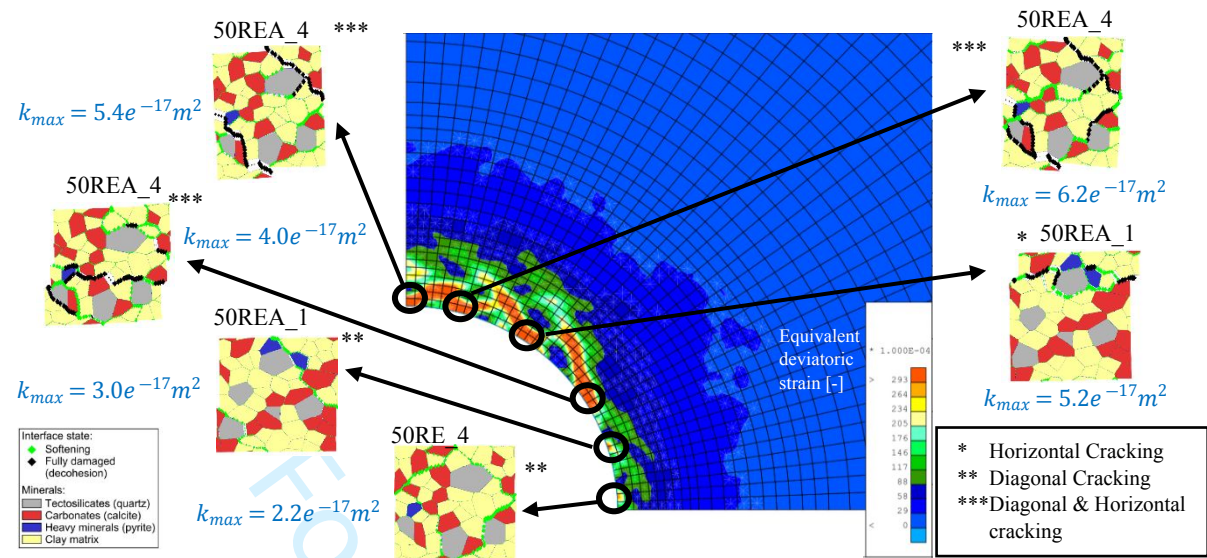*Large-scale failure prediction of clay rock using multiscale modelling*

Figure 31. Strain localisation at the end of excavation and deformed mesostructures in different locations using the 50REA_1, 50REA_2, 50REA_4, and 50REA_5 mesostructures with random distribution (equally in proportion).

Finally, the developed water pressure at different stages during and after the excavation, is illustrated in Figure 32. It can be seen that, at the end of the excavation, there is a small zone above the gallery wall that presents negative water pressure, reaching p_w = -0.1 MPa. This zone corresponds to an area where macro strain localisation develops and where the REAs present mixed and severe fracture modes (see Figure 31). This leads to a dilatant behaviour of the material and pore pressure decrease. In fact, the mesostructure deformation is due to relative displacements of the minerals (numerical cells), which can cause an increase of the voids (cracks) in the microstructure (REA). However, this negative overpressure decreases after the excavation, due to drainage at gallery wall, and finally fully dissipate. Additionally, the water pressure decreases in the rock further away from the gallery wall as drainage occurs in the long term, after the excavation. Further investigations of the hydromechanical coupling effects should be addressed in future studies. This should also include the evolution of the hydraulic permeability of the rock due to its dilatant behaviour at mesoscale, during the gallery excavation.

Furthermore, the values of the major homogenised hydraulic permeability k_{max} of different REAs are indicated in Figure 31. These permeabilities evolve due to deformation and crack developments, as the interfaces between minerals open. The initial permeability of the undeformed material (by defining a minimum hydraulic interface opening) in this study is $1.0e^{-17}$ m^2. It can be seen that, the permeability has increased especially above the gallery, where intense cracking and strain localisation develop. However, it has to be pointed out that the evolution of permeability remains limited by the 2D model which does not take into account the three dimensional nature of fluid percolation paths[7].
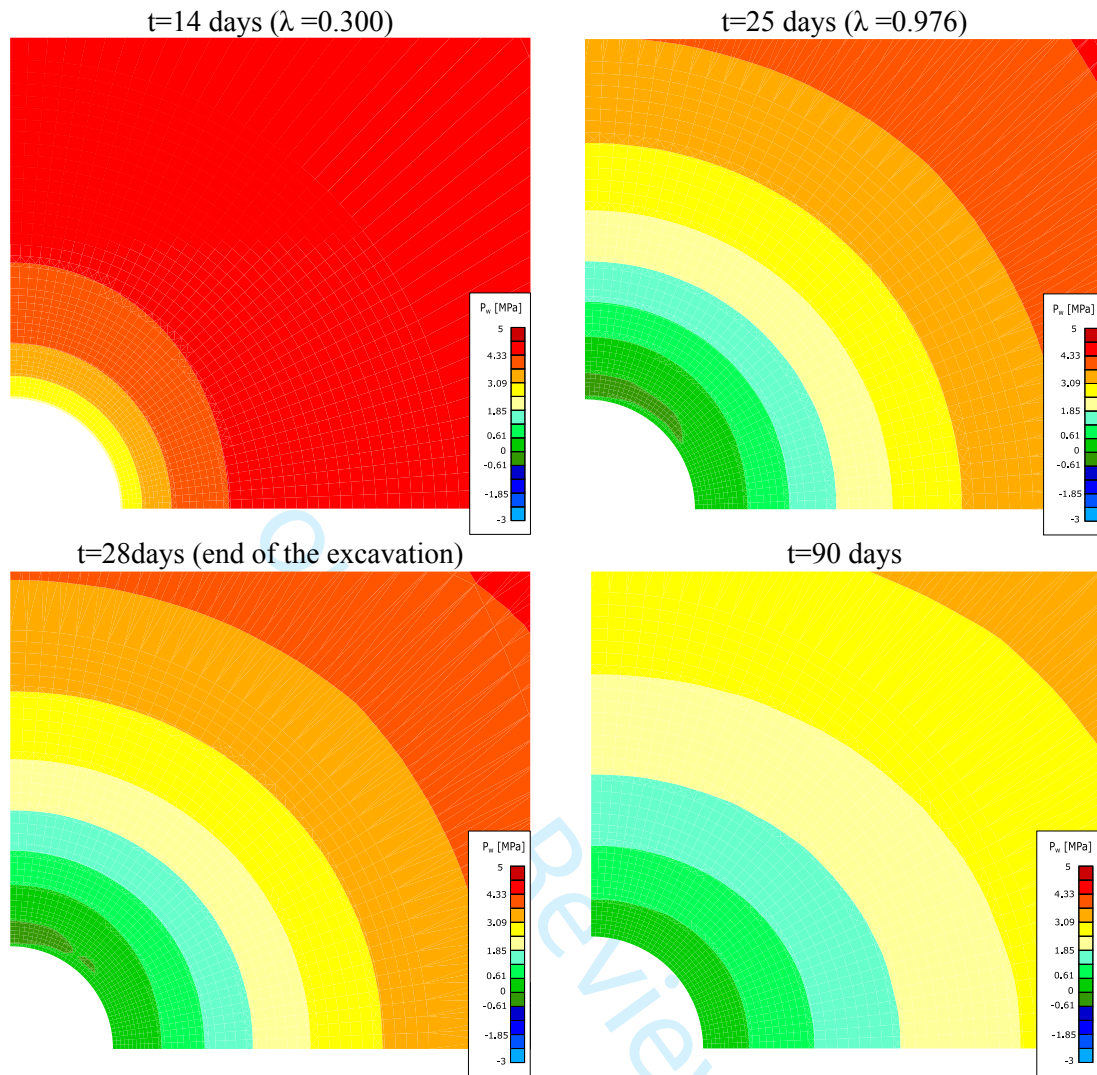
Large-scale failure prediction of clay rock using multiscale modelling

t=14 days (λ =0.300)

t=25 days (λ =0.976)

t=28days (end of the excavation)

t=90 days

Figure 32. Evolution of water pressure during and after the gallery excavation using the 50REA_1, 50REA_2, 50REA_4, and 50REA_5 mesostructures with random distribution (equally in proportion).

7. *Conclusions*

This study demonstrates the ability to reproduce the development of the EDZ induced during gallery excavation, using a double-scale hydro-mechanical (HM) modelling by computational homogeneisation (FE^2), by considering explicitly the heterogeneity at the mesoscale based on the morphology of REAs and mesostructural behaviour. A strategy is proposed in order to predict a clay rock macroscale behaviour and failure by strain localisation. The rock macroscale behaviour (constitutive response) results from the homogenised response of a deformed REA (BVP) that mimic the mesostructure of the material. It is found out that the geometry of REAs, which controls the quantity and the orientation of possible mesocrack (grain debonding or intra-phase cracking), favours some specific coalescence patterns. These preferential cracking paths, identified as primary or secondary inclined orientation, control the induced anisotropy of the REA response after crack coalescence. The latter controls the macroscale constitutive response, especially in highly deformed zones, and influences the possible orientation of the deformation band at macroscale.

The proposed strategy is tested for several mesostructures, having different characteristic sizes (with L_{EA}=50, 70, and 100 μm, i.e. 50, 100, and 250 numerical cells in REAs). Firstly, the REAs behaviour under shearing are studied at mesoscale following a biaxial compression loading. It is concluded that the coalesced mesocrack paths can be well anticipated from a purely geometrical analysis

34

Large-scale failure prediction of clay rock using multiscale modelling

of REA. Then, the shear strength and failure by strain localisation of macroscale digital rock samples are studied under a biaxial compression using previously studied REAs. The comparison shows that the orientation of the developed deformation band is well in adequation with preferential mesocrack path for each case. It has to be highlighted that the anisotropy of the mesostructure, derived mainly by the grain morphology, is the main factor affecting the shear band left or right inclination at macroscale, at least for this homogeneous macroscale BVP.

Furthermore, an intermediate heterogeneity between the mesoscale and macroscscale is studied. It consists in introducing a non-homogeneous distribution of several REAs at each Gauss point of the macroscopic problem. This approach tends to take into account a dispersion of characteristics observed in natural materials. By such a way, a competition study is discussed in order to examine the mesoscale parameters that lead to the development of different shear band orientations, following the preferential mesocracks coalescence tendency of the REAs. It is found out that, the difference in stiffness of each REA triggers the development of shear strain localisations. Two localisation stages appear: the first well before the stress peak in a multiple band pattern, the last around the stress peak, with essentially one or a few dominant bands. This is similar to recent experimental observations based on in situ full field measurements on a clay rock and a porous rock. Therefore, the weaker REAs in terms of stiffness and shear strength attract significant strain localisations. However, if one REA reaches shear failure under a lower strain than others, then it also reaches its strain softening post-peak behaviour earlier. This leads to strain localisations in areas occupied by cluster of weaker REA. Additionally, similar competition studies are conducted using one REA and its symmetrical mirror REA. This way, the two REAs present the exact same stress-strain behaviour but they have an opposite mesocrack path orientation (reverse anisotropy). It can be seen that these analyses develop shear bands in macroscale rock samples with an orientation which is affected by the mesocrack tendency of the REAs. Additionally, the study presents the water pressure evolution in the strain localisation zone, during the modelling of the biaxial compression laboratory test. The hydraulic permeability increase is also shown in mesostructures undergoing mesocracking.

Finally, a gallery excavation is modelled to study the development of the excavation damage zone (EDZ) and the relation between macro and meso deformations. Various REAs are examined in order to test the ability of the double-scale approach to capture the EDZ around galleries by strain localisation. Furthermore, it is derived from this investigation that the use of different REAs (random distribution) with different stiffnesses and shear strengths can trigger the development of strain localisations, especially in areas where the weaker REAs in terms of shear strength are located. In addition, the developed EDZ near the top of the gallery includes REAs with mixed-mode fractures (opening and shear fracture modes) which agrees with the fractures observed in the EDZ around galleries of the Andra URL [6,46]. It can be observed that the EDZ is reasonably reproduced compared to the experimental evidence derived by measurements of fractures around deep galleries in COx clay rock. In particular, the use of several REAs with different mesostructural behaviours and morphologies, which could improve the representativeness of the COx clay rock behaviour, triggers the development of shear bands. These shear bands develop preferentially in the direction of the minor principal stress in the gallery section, as observed in situ around galleries[6,46]. Finally, the evolution of water pressure and of permeability in several REAs inside the shear bands are presented. The results indicate that the mesoscale volumetric behaviour of the material is affecting its hydraulic properties.

The presented modelling approach enlightens the possibility of using computational double-scale modelling for engineering applications, while considering mechanical and morphological information of the geomaterial mesostructure. The approach also investigates the role of an intermediate heterogeneity between macro and mesoscale on the failure pattern by strain localisation. Furthermore, a deeper study on the occurrence and significance of hydro-mechanical coupling phenomena should be considered in a future work as well as a more realistic consideration of heterogeneities at the intermediary scale.

35

Large-scale failure prediction of clay rock using multiscale modelling

References

1. Yven B, Sammartino S, Geraud Y, Homand F, Villieras F. Mineralogy, texture and porosity of Callovo-Oxfordian argillites of the Meuse/Haute-Marne region (eastern Paris Basin). *Bulletin de la Societe Geologique de France, Mém Soc géol France*. 2007;178:73–90.

2. Andra. *Dossier 2005 Argile. Synthesis: Evaluation of the Feasibility of a Geological Repository in an Argillaceous Formation, Meuse/Haute Marne Site. Tech. Rep., Paris.*; 2005.

3. Wileveau Y, Bernier F. Similarities in the hydromechanical response of Callovo-Oxfordian clay and Boom Clay during gallery excavation. *Physics and Chemistry of the Earth, Parts A/B/C*. 2008;33(SUPPL. 1):S343-S349. doi:10.1016/J.PCE.2008.10.033

4. Bossart P, Meier PM, Moeri A, Trick T, Mayor JC. Geological and hydraulic characterisation of the excavation disturbed zone in the Opalinus Clay of the Mont Terri Rock Laboratory. *Engineering Geology*. 2002;66(1-2):19-38. doi:10.1016/S0013-7952(01)00140-5

5. Desbois G, Höhne N, Urai J, Bésuelle P, Viggiani G. Deformation in cemented mudrock (Callovo-Oxfordian Clay) by microcracking, granular flow and phyllosilicate plasticity: Insights from triaxial deformation, broad ion beam polishing and scanning electron microscopy. *Solid Earth*. 2017;8(2):291-305. https://doi.org/10.5194/SE-8-291-2017.

6. Armand G, Leveau F, Nussbaum C, et al. Geometry and Properties of the Excavation-Induced Fractures at the Meuse/Haute-Marne URL Drifts. *Rock Mechanics and Rock Engineering*. 2014;47(1):21-41. https://doi.org/10.1007/S00603-012-0339-6.

7. Eijnden AP van den, Bésuelle P, Collin F, Chambon R, Desrues J. Modeling the strain localization around an underground gallery with a hydro-mechanical double scale model; effect of anisotropy. *Computers and Geotechnics*. 2017;85:384-400. https://hal.univ-grenoble-alpes.fr/hal-01956958.

8. Borja RI. *Multiscale and Multiphysics Processes in Geomechanics (Results of the Workshop on Multiscale and Multiphysics Processes in Geomechanics, Stanford, June 23-25)*. Springer S. Berlin, Heidelberg: Springer Berlin Heidelberg; 2010. https://doi.org/10.1007/978-3-642-19630-0.

9. Dormieux L, Ulm F-J. *Applied Micromechanics of Porous Materials*. Springer; 2005. https://doi.org/10.1007/3-211-38046-9.

10. Hicher P-Y. *Multiscale Geomechanics : From Soil to Engineering Projects*. Wiley-ISTE; 2011.

11. Galvanetto U, Aliabadi MHF. *Multiscale Modeling in Solid Mechanics: Computational Approaches*. Imperial College Press.; 2009. https://doi.org/10.1142/P604.

12. Geers MGD, Kouznetsova VG, Brekelmans WAM. Multi-scale computational homogenization: Trends and challenges. *Journal of Computational and Applied Mathematics*. 2010;234(7):2175-2182. https://doi.org/10.1016/J.CAM.2009.08.077.

13. Kouznetsova V, Brekelmans WAM, Baaijens FPT. An approach to micro-macro modeling of heterogeneous materials. *Computational Mechanics*. 2001;27(1):37-48. https://doi.org/10.1007/S004660000212.

14. Frey J, Chambon R, Dascalu C. A two-scale poromechanical model for cohesive rocks. *Acta Geotechnica*. 2012;8(2):107-124. https://doi.org/10.1007/S11440-012-0173-8.

15. van den Eijnden AP, Bésuelle P, Chambon R, Collin F. A FE2 modelling approach to hydromechanical coupling in cracking-induced localization problems. *International Journal of Solids and Structures*. 2016;97_98:475-488. https://doi.org/10.1016/J.IJSOLSTR.2016.07.002.

16. Pardoen B, Bésuelle P, Dal Pont S, Cosenza P, Desrues J. Accounting for Small-Scale Heterogeneity and Variability of Clay Rock in Homogenised Numerical Micromechanical Response and Microcracking. *Rock Mechanics and Rock Engineering*. 2020;53(6):2727-2746. https://doi.org/10.1007/s00603-020-02066-7.

17. Tsang C-F, Bernier F, Davies C. Geohydromechanical Processes in the Excavation Damaged Zone in Crystalline Rock, Rock Salt, and Indurated and Plastic Clays Publication Date.

Large-scale failure prediction of clay rock using multiscale modelling

1   *International Journal of Rock Mechanics and Mining Sciences*. 2004;42(1):109-125.
2   https://escholarship.org/uc/item/0xk809dg.

18. Emsley S, Olsson O, Stenberg L, Alheid HJ, Falls S. *ZEDEX - A Study of Damage and
Disturbance from Tunnel Excavation by Blasting and Tunnel Boring. Svensk
Kärnbränslehantering AB/Swedish Nuclear Fuel and Waste Management Co.*; 1997.
http://inis.iaea.org/Search/search.aspx?orig_q=RN:29050588.

19. Gaucher EC, Robelin C, Matray J., et al. ANDRA underground research laboratory:
interpretation of the mineralogical and geochemical data acquired in the Callovian-Oxfordian
formation by investigative drilling. *Physics and Chemistry of The Earth*. 2004;29(1):55-77.
https://doi.org/10.1016/J.PCE.2003.11.006.

20. Robinet J-C, Sardini P, Coelho D, et al. Effects of mineral distribution at mesoscopic scale on
solute diffusion in a clay-rich rock: Example of the Callovo-Oxfordian mudstone (Bure, France).
Water Resources Research. 2012;48(5). https://doi.org/10.1029/2011WR011352.

21. Cosenza P, Prêt D, Zamora M. Effect of the local clay distribution on the effective electrical
conductivity of clay rocks. *Journal of Geophysical Research: Solid Earth*. 2015;120(1):145-168.
https://doi.org/10.1002/2014JB011429.

22. Cosenza P, Prêt D, Giraud A, Hedan S. Effect of the local clay distribution on the effective elastic
properties of shales. *Mechanics of Materials*. 2015;84:55-74.
https://doi.org/10.1016/J.MECHMAT.2015.01.016.

23. Pardoen B, Collin F, Bésuelle P, et al. Modelling the multiscale behaviour of claystone:
deformation, rupture, and hydro-mechanical phenomena around underground galleries. *In JS
McCartney and I Tomac (Eds) 2nd International Conference on Energy Geotechnics (ICEGT)
E3S Web of Conferences 205, 10003*. 2020;205:10003. doi:10.1051/E3SCONF/202020510003

24. Pardoen B, Dal Pont S, Desrues J, Bésuelle P, Prêt D, Cosenza P. Heterogeneity and Variability
of Clay Rock Microstructure in a Hydro-Mechanical Double Scale FEM × FEM Analysis. *In:
Giovine P, Mariano P, Mortara G (Eds) Micro to MACRO Mathematical Modelling in Soil
Mechanics (pp 247-256) Trends in Mathematics Birkhäuser, Cham, Springer*. 2018.
doi:10.1007/978-3-319-99474-1_25.

25. Desrues J, Argilaga A, Caillerie D, et al. From discrete to continuum modelling of boundary
value problems in geomechanics: An integrated FEM-DEM approach. *International Journal for
Numerical and Analytical Methods in Geomechanics*. 2019;43(5):919-955.
https://doi.org/10.1002/NAG.2914.

26. Jenny P, Lee SH, Tchelepi HA. Adaptive fully implicit multi-scale finite-volume method for
multi-phase flow and transport in heterogeneous porous media. *Journal of Computational
Physics*. 2006;217(2):627-641. https://doi.org/10.1016/J.JCP.2006.01.028.

27. Zhang Q, Yao J, Huang Z, Li Y, Zhang K. Hybrid multiscale method for numerical modeling of
coupled flow and geomechanics. *Journal of Petroleum Science and Engineering*. 2019;176:943-
951. https://doi.org/10.1016/10.1016/J.PETROL.2019.02.009.

28. Etse G, Caggiano A, Vrech S. Multiscale failure analysis of fiber reinforced concrete based on a
discrete crack model. *International Journal of Fracture*. 2012;178(1):131-146.
https://doi.org/10.1007/S10704-012-9733-Z.

29. García-Macías E, Guzmán CF, Saavedra Flores EI, Castro-Triguero R. Multiscale modeling of
the elastic moduli of CNT-reinforced polymers and fitting of efficiency parameters for the use
of the extended rule-of-mixtures. *Composites Part B: Engineering*. 2019;159:114-131.
https://doi.org/10.1016/J.COMPOSITESB.2018.09.057.

30. Watanabe I, Sun Z, Kitano H, Goto K. Multiscale analysis of mechanical behavior of multilayer
steel structures fabricated by wire and arc additive manufacturing. *Science and technology of
advanced materials*. 2020;21(1):461-470. https://doi.org/10.1080/14686996.2020.1788908.

31. Chambon R, Caillerie D, Matsuchima T. Plastic continuum with microstructure, local second
gradient theories for geomaterials: localization studies. *International Journal of Solids and
Structures*. 2001;38(46-47):8503-8527. doi:10.1016/S0020-7683(01)00057-9

32. Collin F, Chambon R, Charlier R. A finite element method for poro mechanical modelling of
geotechnical problems using local second gradient models. *International Journal for Numerical
Methods in Engineering*. 2006;65(11):1749-1772. https://doi.org/10.1002/NME.1515.

33. Pardoen B, Collin F. Modelling the influence of strain localisation and viscosity on the behaviour

37

of underground drifts drilled in claystone. *Computers and Geotechnics*. 2017;85:351-367. https://doi.org/10.1016/J.COMPGEO.2016.05.017.

34. Mindlin RD. Second gradient of strain and surface-tension in linear elasticity. *International Journal of Solids and Structures*. 1965;1(4):417-438. https://doi.org/10.1016/0020-7683(65)90006-5.

35. Germain P. The Method of Virtual Power in Continuum Mechanics. Part 2: Microstructure. *SIAM Journal on Applied Mathematics*. 2006;25(3):556-575. https://doi.org/10.1137/0125053.

36. Chambon R, Caillerie D, El Hassan N. One-dimensional localisation studied with a second grade model. *European Journal of Mechanics, A/Solids*. 1998;17(4):637-656. https://doi.org/10.1016/S0997-7538(99)80026-6.

37. Matsushima T, Chambon R, Caillerie D. Large strain finite element analysis of a local second gradient model: Application to localization. *International Journal for Numerical Methods in Engineering*. 2002;54(4):499-521. https://doi.org/10.1002/NME.433.

38. Kotronis P, Collin F, Chambon R, et al. Local Second Gradient Models and Damage Mechanics: 1D Post-Localization Studies in Concrete Specimens. In: *Bifurcation, Instabilities and Degradation in Geomechanics*. Bifurcation, Instabilities and Degradation in Geomechanics, Springer Berlin Heidelberg; 2007:127–142. https://doi.org/10.1007/978-3-540-49342-6_6ï.

39. Collin F, Caillerie D, Chambon R. Analytical solutions for the thick-walled cylinder problem modeled with an isotropic elastic second gradient constitutive equation. *International Journal of Solids and Structures*. 2009; 46(22-23):3927-3937. https://doi.org/10.1016/J.IJSOLSTR.2009.05.017.

40. Charlier R. *Approche Unifiée de Quelques Problèmes Non Linéaires de Mécanique Des Milieux Continus Par La Méthode Des Éléments Finis : Grandes Déformations Des Métaux et Des Sols, Contact Unilatéral de Solides, Conduction Thermique et Écoulements En Milieux Poreux.*; 1987. https://books.google.fr/books/about/Approche_unifiée_de_quelques_problèmes.html?id=w_R1 zgEACAAJ&redir_esc=y.

41. Mandel J. Plasticité classique et viscoplasticité. *CISM lecture notes, 97.* 1972.

42. Hill R. A self-consistent mechanics of composite materials. *Journal of the Mechanics and Physics of Solids*. 1965;13(4):213-222. https://doi.org/10.1016/0022-5096(65)90010-4.

43. Pardoen B, Seyedi DM, Collin F. Shear banding modelling in cross-anisotropic rocks. *International Journal of Solids and Structures*. 2015;72:63-87. https://doi.org/10.1016/J.IJSOLSTR.2015.07.012.

44. Pardoen B, Bésuelle P, Dal Pont S, Cosenza P, Desrues J. Effect of claystone small-scale characteristics on the variability of micromechanical response and on microcracking modelling. *In: Barla, M, Di Donna, A, Sterpi, D (Eds) Challenges and innovations in geomechanics 16th International Conference of the International Association for Computer Methods and Advances in Geomechanics (IACMAG)*. 2021.

45. Bésuelle P, Chambon R, Collin F. Switching deformation modes in post-localization solutions with a quasibrittle material. *Journal of Mechanics of Materials and Structures*. 2006;1(7):1115-1134. doi:10.2140/JOMMS.2006.1.1115

46. Armand G, Conil N, Talandier J, Seyedi DM. Fundamental aspects of the hydromechanical behaviour of Callovo–Oxfordian claystone: from experimental studies to model calibration and validation. *Computers and Geotechnics*. 2017; C(85):277-286. https://doi.org/10.1016/J.COMPGEO.2016.06.003.

47. Couture C, Bésuelle P. A true triaxial experimental study on porous Vosges sandstone: from strain localization precursors to failure using full-field measurements. *International Journal of Rock Mechanics and Mining Sciences*. 2022; 153:105031. doi:10.1016/J.IJRMMS.2021.105031.

48. Bésuelle P. Caractérisation du comportement anisotrope de l'argilite du Callovo-Oxfordien. *Technical Report, ANDRA,* Grenoble. *2021*.

49. Pardoen B, Levasseur S, Collin F. Using Local Second Gradient Model and Shear Strain Localisation to Model the Excavation Damaged Zone in Unsaturated Claystone. *Rock Mechanics and Rock Engineering*. 2015;48(2):691-714. https://doi.org/10.1007/S00603-014-0580-2.

50. Zervos A, Papanastasiou P, Vardoulakis I. Modelling of localisation and scale effect in thick-walled cylinders with gradient elastoplasticity. *International Journal of Solids and Structures*. 2001;38(30-31):5081-5095. https://doi.org/10.1016/S0020-7683(00)00337-1.

38